Chemical Geology 579 (2021) 120242

Contents lists available at ScienceDirect

Chemical Geology

journal homepage: www.elsevier.com/locate/chemgeo

Tracing sulfur sources in the crust via SIMS measurements of sulfur isotopes in apatite

Johannes Hammerli [a,b,*], Nicolas D. Greber [a,c], Laure Martin [d], Anne-Sophie Bouvier [e], Anthony I.S. Kemp [f], Marco L. Fiorentini [b], Jorge E. Spangenberg [g], Yuichiro Ueno [h,i], Urs Schaltegger [c]

[a] Institute of Geological Sciences, University of Bern, Baltzerstrasse 1+3, 3012 Bern, Switzerland
[b] Centre for Exploration Targeting, ARC Research Council Centre of Excellence for Core to Crust Fluid Systems (CCFS), The University of Western Australia, Perth, 6009, Australia
[c] Department of Earth Sciences, University of Geneva, 13 rue des Maraîchers, 1205 Geneva, Switzerland
[d] Centre for Microscopy, Characterisation and Analysis, The University of Western Australia, Perth, WA 6009, Australia
[e] Institute of Earth Sciences, University of Lausanne, CH1015 Lausanne, Switzerland
[f] School of Earth Sciences, The University of Western Australia, Crawley, Australia
[g] Institute of Earth Surface Dynamics, University of Lausanne, CH1015 Lausanne, Switzerland
[h] Department of Earth and Planetary Sciences, Tokyo Institute of Technology, Meguro, Tokyo 152-8551, Japan
[i] Earth-Life Science Institute (WPI-ELSI), Tokyo Institute of Technology, Meguro, Tokyo 152-8550, Japan

ARTICLE INFO

Keywords:
Sulfur isotopes in apatite
SIMS sulfur isotope analysis
Multiple S isotope analysis in apatite
Tracing S in the crust
New reference material for S isotope analysis in apatite

ABSTRACT

We present a refined approach for acquiring sulfur (S) isotope compositions ($^{33}S/^{32}S$, $^{34}S/^{32}S$) in apatite by secondary ion mass spectrometry (SIMS), including the characterisation of new reference materials. In order to test the method, we analyzed potential apatite reference samples for their S isotope ratios via three different bulk methods. The investigated apatite samples contain S concentrations between ~160 μg/g and 3100 μg/g and their $^{34}S/^{32}S$ ($\delta^{34}S$) ratios deviate by more than 25‰ from the Vienna-Canyon Diablo Troilite (VCDT) standard. We identified four candidates as new primary reference materials for routine SIMS S isotope measurements of apatite. Based on ICP-MS, EA-IRMS, and fluorination analyses, recommended S isotope values are +12.27± 0.22 (2σ) ‰ $\delta^{34}S$ for SAP1, +14.02 ± 0.22 (2σ) ‰ $\delta^{34}S$ for Big1, −1.06 ± 0.80 (2σ) ‰ $\delta^{34}S$ for Durango-A, and −1.39 ± 0.48 (2σ) ‰ for Durango-B. By selecting one of those four primary standards for SIMS analysis, the S isotope values of the other reference materials and additional tested apatite specimens can be reproduced to within 1‰. Under optimized SIMS conditions, single spot uncertainty for $\delta^{34}S$ that combines the within-spot precision and the repeatability of measurements of the primary apatite reference material during an analytical session is ±0.4‰ (95% CI). We also show that in apatite with S > 1000 μg/g, SIMS analysis permits the detection of mass-independent S isotope signatures (i.e., $\Delta^{33}S$) that are larger than ~1.0‰ if an average of multiple grains is used, and larger than ~1.5‰ for a single analytical point. Furthermore, our study shows that apatite can record S isotope signatures from extremely diverse environments, making this near-ubiquitous mineral a key candidate for tracing S source reservoirs and to track the pathway of magmatic-hydrothermal fluids in a wide range of geological settings.

1. Introduction

Sulfur has a key role within many first order planetary processes, such as development and evolution of life, core-mantle differentiation (Labidi et al., 2016), the development of Earth's atmosphere (Canfield, 2004), the formation of ore-deposits (e.g., Benning and Seward, 1996), and the redox budget of the mantle (Evans, 2012). Sulfur isotope analyses in bulk rock samples, sulfide and sulfate minerals, have significantly improved our understanding of these processes (e.g., Chaussidon et al., 1989; Farquhar et al., 2000, 2002; Hattori and Keith, 2001; Farquhar and Wing, 2003; Ono et al., 2006; Kozdon et al., 2010; Ushikubo et al., 2014; Marin-Carbonne et al., 2020), especially as S isotopes

* Corresponding author at: Institute of Geological Sciences, University of Bern, Baltzerstrasse 1+3, 3012 Bern, Switzerland.
E-mail address: Johannes.haemmerli@geo.unibe.ch (J. Hammerli).

https://doi.org/10.1016/j.chemgeo.2021.120242
Received 24 December 2020; Received in revised form 7 April 2021; Accepted 8 April 2021
Available online 15 April 2021

exhibit variations due to both mass dependent and mass independent fractionation. The former is expressed as $\delta^{34}S$, which is the deviation in parts per thousand (‰) of the $^{34}S/^{32}S$ ratio relative to the Vienna Canyon Diablo Troilite (VCDT) standard. In contrast, mass independent S isotope fractionation (MIF, reported as $\Delta^{33}S$ or $\Delta^{36}S$) represents the deviations of the $^{33}S/^{32}S$ ($\Delta^{33}S$) and $^{36}S/^{32}S$ ($\Delta^{36}S$) ratios from the normal mass dependent relationship.

The strength of the S isotope tracer is that relatively large mass dependent isotope fractionation occurs in Earth's surface environments and during biological metabolisms. As a consequence, different reservoirs, such as Earth's mantle ($\delta^{34}S \sim 0$‰) or modern seawater ($\delta^{34}S$ of around +20‰), have distinct S isotope compositions (Fig. 1). Sulfur isotope studies can therefore trace S sources (i.e., S-bearing fluids) to constrain and understand S transfer between the deep Earth, its surface environments, and the biosphere. The anomalous S isotope signatures produced by mass independent fractionation are important for tracing the history of the oxygenation of the Earth's atmosphere (Farquhar et al., 2000, 2010) and for tracking ancient S reservoirs in the deep Earth (e.g., Delavault et al., 2016). The advantage of high spatial resolution SIMS analyses compared to bulk mineral S isotope measurements is that the textural context of the S-bearing phases in the rock can be retained. Different generations of S-bearing fluid-rock interaction can be resolved within a sample or even within a single mineral on a micrometer scale, for example, to distinguish between open and closed systems and different fluid sources in subduction zones (Evans et al., 2014; Giacometti et al., 2014), or to track the change of sulfide precipitation from a high temperature vapor phase to a low temperature liquid fluid phase (e.g., Tanner et al., 2016).

While sulfides and sulfates are the most routinely analyzed minerals for S isotope ratios on a sub-mineral scale (e.g., Whitehouse, 2013; LaFlamme et al., 2016; Magnall et al., 2016), other S-bearing minerals, such as scapolite or apatite, are promising for constraining S sources and S cycling in a wide range of rock types (Hammerli et al., 2017; Economos et al., 2017). The mineral apatite, with the general stoichiometric formula of $Ca_5(PO_4)_3(F,Cl,OH)$, has particular utility for S isotope quantification because it can host S as a minor element, is near ubiquitous in crustal rocks, and also occurs in extraterrestrial materials (e.g., Boyce et al., 2010; McCubbin and Jones, 2015 and references therein).

The crystallization of sulfur-rich apatite, which can concentrate several thousands of µg/g sulfur in its crystal lattice, is generally attributed to relatively oxidizing conditions, where S is incorporated as S^{6+}, for example, via the following proposed substitutions (e.g., Parat et al., 2011a, 2011b; Konecke et al., 2019 and references therein):

$$PO_4^{3-} + Ca^{2+} \Leftrightarrow SO_4^{2-} + Na^{+}$$

$$Ca^{2+} + 2PO_4^{3-} \Leftrightarrow 2SO_4^{2-} + [\ ]$$

$$2PO_4^{3-} \Leftrightarrow SO_4^{2-} + SiO_4^{4-}$$

However, recent studies have suggested that S can also be incorporated in its reduced form (S^{2-}) (Konecke et al., 2017, 2019; Brounce et al., 2019; Sadove et al., 2019), which means that apatite might not only be a useful mineral for tracing the source of oxidized fluids, but also for tracing S sources in reduced settings. Another benefit of determining S isotopes in apatite is that the S isotope signature may be linked with U-Pb age constraints of apatite; hence, fluid-rock interaction might be resolved temporally.

Economos et al. (2017) first described the method of in situ SIMS S isotope (^{32}S and ^{34}S to determine $\delta^{34}S$ values) analyses in apatite by using Durango apatite as their internal reference material. Their study showed that significant isotope variations of up to 6‰ in $\delta^{34}S$ can be archived within individual apatite grains. However, one of the remaining limiting factors for routine S isotope analyses in apatite minerals is the lack of additional reference material to monitor the accuracy of the results. This is ideally achieved via several well-characterized apatite samples that cover a large range of S concentrations and S isotope ratios.

In this study, we isotopically characterize and test several apatite samples for their suitability as S isotope standards via three different bulk methods and multiple SIMS sessions. The studied samples contain between ~0.04wt% SO_3 (~160 µg/g S) and 0.78 wt% SO_3 (~3100 µg/g S) and have $\delta^{34}S$ signatures that range over more than 25‰. Pushing the analytical boundaries further, we explore the possibility of adding a third S isotope (^{33}S) to the analytical routine, essential for identifying anomalous S isotope signatures suggestive of mass independent fractionation.

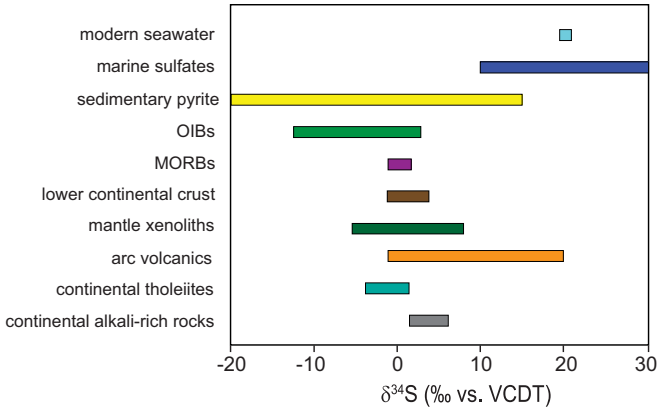

Fig. 1. Sulfur isotope signatures in different terrestrial reservoirs. Marine sulfates/sedimentary pyrite: Farquhar et al. (2010) and references therein. OIBs: Sakai et al. (1984); Torssander (1989); Chaussidon et al. (1989); Cabral et al. (2013). MORBs: Kanehira et al. (1973); Sakai et al. (1984); Labidi et al. (2012, 2013). Lower continental crust: Hammerli et al. (2017). Mantle xenoliths: Chaussidon et al. (1989); Chaussidon & Lorand (1990); Kyser (1990); Ionov et al. (1992); Wilson et al. (1996). Arc Volcanics: Ueda and Sakai (1984); Alt et al. (1993); Woodhead et al. (1987); de Hoog et al. (2001), Marini et al. (2011). Continental tholeiites: Schneider (1970). Continental alkali-rich rocks: Schneider (1970), Harmon et al. (1987).

2. Materials

A total of eight apatite crystals were analyzed for their compositions and S isotope ratios (see section below). Three samples were obtained from the collection of the Natural History Museum Bern, Switzerland (NMBE): Hormuz apatite (NMBE B6634), collected in 1958 from the salt Diapir that is described in Hurford et al., 1984; Durango-B apatite, Cerro de Mercado, Mexico (NMBE A230); Madagascar (Mdg-1) apatite (NMBE 40865) from Milanoa, Madagascar. A second Durango apatite, named Durango-A, originates from the same collection as the one used in the study by Boehnke et al. (2018) for Sr isotope analysis. Four gemstone quality apatite crystals were purchased from online vendors (Big1, SAP1, SAP2, SAP3) and all of them originate also from Madagascar according to the retailer. All analyzed crystals are clear and devoid of inclusions. Their sizes range from ~1 to ~2 cm in length.

3. Analytical methods

3.1. Sample preparation

For euhedral crystals, such as Durango A, Durango B, and Big1, slices of the minerals were cut along, and perpendicular to their C-axis and embedded in 1-in. epoxy mounts. Equal parts of the specimens were then used for bulk analyses (see section 3.3). For non-euhedral minerals, the grains were cut in roughly two halves. One half was embedded in epoxy whereas parts of the other half were used for bulk analyses and smaller pieces were embedded in epoxy mounts together with the rest of the studied apatite grains. In addition, a total of 6 epoxy mounts, each containing several fragments of the respective apatite samples with random crystal orientations relative to the c-axis, were prepared. In the

case of samples SAP1, SAP3, and Big1, >20 individual crystal fragments were mounted in epoxy to further test their homogeneity, in addition to transect analyses. All samples were placed in the central 10 mm of the mount to prevent sample location effects during SIMS analyses (Kita et al., 2011), and subsequently polished stepwise starting from 6 down to 1 μm diamond paste.

3.2. Electron Probe Micro-Analysis (EPMA)

The concentrations of major (Ca, P, Si, F, Cl) and minor elements (Mn, Mg, Fe, Na, S) in the apatite samples were determined via electron probe microanalysis (EPMA) using a JEOL JXA 8200 superprobe at the Institute of Geological Sciences, University of Bern, Switzerland. The analytical potential was set at 15 kV and 10 nA beam current. Counting times were 10 s on peak and 20 s on background for each element, besides for S, which was counted for 30 s on peak. The data were processed using ZAF corrections and standardized via in-house standards (apatite for P_2O_5 and CaO, magnetite for FeO, celestine for SO_3, topaz for F, orthoclase for SiO_2, tugtupite for Cl, forsterite for Mg, albite for Na, and spessartine for MnO). The stoichiometry of the unknowns was calculated according to Ketcham (2015).

3.3. Bulk sulfur isotope analyses

Bulk analyses of the eight potential new apatite reference materials were performed via three different methods. SAP1, SAP2, and Big1 were analyzed via the fluorination method at Tokyo Institute of Technology (Japan) and by solution multi-collector inductively coupled mass spectrometry (MC-ICP-MS) analyses at the Universities of Geneva and Bern (Switzerland). Durango-A and Durango-B were analyzed by elemental analysis-isotope ratio mass spectrometry (EA-IRMS) at the University of Lausanne (Switzerland), whereas Durango-B was also measured via solution MC-ICP-MS analyses. Hormuz, SAP3, and Mdg-1 apatite were analyzed via solution MC-ICP-MS. Mass-dependent S isotope compositions are reported throughout this manuscript in the delta-notation, as per mil (‰) deviation in the $^{3x}S/^{32}S$ ratio from the VCDT reference, with ^{3x}S being ^{33}S ($\delta^{33}S$), ^{34}S ($\delta^{34}S$) or ^{36}S ($\delta^{36}S$).

3.3.1. Multiple sulfur isotope analysis by the fluorination method

Multiple sulfur isotope analyses (^{32}S, ^{33}S, ^{34}S, ^{36}S) for three bulk apatite samples (SAP1, SAP2, and Big1) were conducted by the fluorination method (Ueno et al., 2015) at Tokyo Institute of Technology. First, powder aliquots of the bulk apatite samples were rinsed with 10 wt % NaCl water for 24h in order to remove water soluble sulfate not included in the apatite crystal lattice. The samples were then filtered through a glass fiber filter (0.3 μm). To ensure the complete removal of the soluble sulfate other than apatite, 1 mL of 1 M $BaCl_2$ was added into the remaining solution to monitor $BaSO_4$ precipitate from gypsum and anhydrite. The rinse was repeated twice to ensure that there was no $BaSO_4$ precipitate. Subsequently, the rinsed apatite sample was further washed with pure acetone for 24 h to remove, if present, any elemental sulfur (e.g., as a result of oxidation of pyrite micro-inclusions contained in the sample). After the treatments with NaCl, $BaCl_2$ and acetone, the washed apatite sample was digested with 6 M HCl to extract sulfate in apatite. The solution was titrated with a NaOH solution to pH 2–3, and following this step, a 1 M $BaCl_2$ solution was added to precipitate the dissolved sulfate as $BaSO_4$. After 12 h, the $BaSO_4$ was filtered, further rinsed with pure acetone, and then dried overnight. Afterwards, the $BaSO_4$ was converted into H_2S by using tin(II) phosphate solution at 350 °C under a N_2 stream (Kiba et al., 1955). The H_2S gas was then introduced into an $AgNO_3$ solution and converted to Ag_2S. The Ag_2S was rinsed with distilled water and dried in an oven at 90 °C overnight.

Quadruple sulfur isotope analysis was carried out by a flash fluorination method (Ueno et al., 2015). The Ag_2S samples and CoF_3 were wrapped in a thin foil that consists of iron-nickel-cobalt alloy (Pyrofoil) with a 590 °C Curie-point temperature. The sample was heated for 3 s by a Curie-point pyrolyzer (JHP-22, Japan Analytical Industry Co., Ltd.) to convert the Ag_2S into SF_6. Product SF_6 was first collected in a cold trap at −196 °C for removing non-condensable gasses including F_2. Then, HF and other byproducts were removed by a second cold trap maintained at −90 °C. The pre-treated SF_6 was further purified by gas chromatography (Shimazu GC8A) equipped with the first 4 m column packed with Porapack-Q (1/8″ OD, 80–100 mesh) connected with the second 3 m Molecular Sieves 5A column (1/8″ OD, 60–80 mesh) at 50 °C oven temperature and a 25 mL/min He flow rate. Purified SF_6 was introduced into a mass spectrometer (Thermo Fisher Scientific, MAT253) and abundances of $^{32}SF_5^+$, $^{33}SF_5^+$, $^{34}SF_5^+$ and $^{36}SF_5^+$ were measured in a dual inlet mode.

Sulfur isotopic compositions are reported as:

$$\delta^{34}S = \left({}^{34}R_{sample}/{}^{34}R_{VCDT} - 1\right) \quad (1)$$

$$\Delta^{33}S = \left[{}^{33}R_{sample}/{}^{33}R_{VCDT} - \left({}^{34}R_{sample}/{}^{34}R_{VCDT}\right)^{0.515}\right] \quad (2)$$

$$\Delta^{36}S = \left[{}^{36}R_{sample}/{}^{36}R_{VCDT} - \left({}^{34}R_{sample}/{}^{34}R_{VCDT}\right)^{1.90}\right] \quad (3)$$

where ^{33}R, ^{34}R, and ^{36}R represent $^{33}S/^{32}S$, $^{34}S/^{32}S$ and $^{36}S/^{32}S$ ratios, respectively. All delta values (in per mil, ‰) were calibrated against the VCDT scale using the IAEA-S1 standard ($\delta^{34}S = -0.30‰$, $\Delta^{33}S = +0.100‰$, $\Delta^{36}S = -0.91‰$; Ding et al., 2001; Ono et al., 2006). Analytical precision determined by replicate analysis of the sample and the standard is better than ±0.24‰ (2 standard error (SE)) for $\delta^{34}S$, ±0.12‰ (2SE) for $\delta^{33}S$, ±0.01‰ (2SE) for $\Delta^{33}S$, and ± 0.24‰ (2SE) for $\Delta^{36}S$ (see supplementary table A-1).

3.3.2. Elemental analysis – Isotope ratio mass spectrometry (EA-IRMS)

To determine the bulk apatite $\delta^{34}S$ value by EA-IRMS, aliquots of the apatite crystals were first completely digested in distilled 3 M HCl at 80 °C for a day and then mixed with concentrated $BaCl_2$ solution to precipitate the S in the form of barium sulphate ($BaSO_4$) (Benmore et al., 1983; Shields et al., 1999). The $BaSO_4$ was then removed from the sample solution by centrifugation and washed three times with MilliQ water to remove leftover acid and coprecipitate $BaCl_2$. The dried $BaSO_4$ was analyzed for their S isotope compositions at the University of Lausanne with a Carlo Erba 1108 elemental analysis system (EA, Fisons Instruments, Milan, Italy) connected to a Thermo Fisher Scientific (Bremen, Germany) Delta V Plus isotope ratio mass spectrometry device (IRMS) following the protocol of Spangenberg et al. (2010). A 3-point calibration with three international reference materials using the currently recommended values after Brand et al. (2014) was performed: NBS-127 ($\delta^{34}S = +21.12 \pm 0.22‰$), IAEA-SO-5 ($\delta^{34}S = +0.49 \pm 0.11‰$) and IAEA-SO-6 ($\delta^{34}S = -34.05 \pm 0.08‰$). Phosphate geostandard BCR-32 (lot nr.1562) was processed together with the samples and yielded a $\delta^{34}S$ value of +20.2 ± 0.8 (2SD, $n = 4$). This is identical within the 2-sigma error but on average slightly higher than the published value of +18.8 ± 1.0‰ (2SD) by Goedert et al. (2016). Consequently, we estimate the uncertainties for analyses of the apatite samples from repeated analyses of standard reference material BCR-32 of ±0.8‰. BCR-32 is not a certified S isotope standard and different batches/lot numbers of this material might have slightly different S isotope compositions. Unfortunately, we were not able to obtain a sample aliquot from the same batch used by Goedert et al. (2016).

3.3.3. MC-ICP-MS

To determine the S isotope composition by the fluorination method or EA-IRMS, ideally more than 1 mg of $BaSO_4$ has to be available for the analysis. However, obtaining this amount of $BaSO_4$ from apatites of low S concentrations, such as Mdg-1 (~160 μg/g) and Hormuz (~280 μg/g) was not achievable with the amount of material we had available. We therefore analyzed the S isotope composition of apatite samples Mdg-1, Hormuz and also SAP1, SAP2, SAP3, Big1, and Durango-B by a Thermo-

Scientific Neptune MC-ICP-MS at the Universities of Geneva and Bern in solution mode. As with S isotope analyses using EA-IRMS, aliquots of the apatite crystals were completely dissolved in 3 M HCl, then mixed with concentrated $BaCl_2$ solution to precipitate $BaSO_4$, which was then isolated and purified by centrifuge. $BaSO_4$ was then leached for 24 h in 1 M HNO_3. The leachate was subsequently diluted with 0.3 M HNO_3 in order to obtain S concentrations that generate around 10 V for the ^{32}S signal on the Neptune MC-ICP-MS (relative to a 10^{11} Ω resistor). The phosphate geostandard BCR-32 was prepared in the same way as the apatite samples. As the bracketing standard and as a secondary standard, we used the barite sulfur isotope reference materials NBS-127 and IAEA-SO-5, respectively. Both of these standards were also leached in 1 M HNO_3 and subsequently diluted prior to analyses by MC-ICP-MS. This approach ensured matrix matching between samples and bracketing standards.

The S isotope composition was then analyzed using a Neptune MC-ICP-MS, simultaneously measuring the masses 32, 33, and 34 in faraday cups. As all of the isotopes are affected by polyatomic interferences (e.g., $^{16}O_2$ and $^{17}O_2$ on ^{32}S and ^{34}S), the measurements were performed in high-resolution mode on the interference-free peak shoulders. For the interface, X skimmer and Jet sampler cones were used, and the sample was introduced with an Aridus II desolvating nebulizer system. Data reduction included an on-peak zero baseline correction and instrumental isotope fractionation was corrected for with the sample-standard bracketing method using barite reference material NBS-127 as standard. With this method, barite reference material IAEA-SO-5 and phosphate BCR-32 yielded $\delta^{34}S$ values of +0.7 ± 0.4‰ (2SD) ($n = 6$) and +20.8 ± 0.6‰ (2SD) ($n = 5$). The value obtained for IAEA-SO-5 agrees with the recommended value (i.e. +0.49‰, Brand et al., 2014) and the value obtained for BCR-32 agrees with that measured by EA-IRMS (see above and supplementary table A-2). All the samples were measured 2 to 4 times from the same sample aliquot. Uncertainties are best estimated by the 2SD of the secondary standards BCR-32 and IAEA-SO-05, which is ±0.6‰ for $\delta^{34}S$ values and ± 0.3‰ for $\delta^{33}S$ values ($n = 11$).

3.3.4. SIMS analysis

Eight different apatite specimens were tested for their isotopic homogeneity in two different SIMS laboratories. The slightly different instrumentation set-ups in the two laboratories allowed for a robust testing of the suitability of reference material for routine SIMS analyses. For example, at the Centre for Microscopy, Characterisation and Analysis (CMCA) at the University of Western Australia (UWA), S isotopes were measured via two Faraday cups (FC) for ^{32}S and ^{34}S and an electron multiplier (EM) for ^{33}S, while at the SwissSIMS facility one FC (^{32}S) and one EM (^{34}S) was used, the latter allowing the detection of ^{34}S in apatite specimens with low S contents (Hormuz, Mdg-1) (see below). Several different mounts were prepared, some of which contained large pieces of the individual specimens for testing their homogeneity via transects, while other mounts contained several fragments of all samples or a subset of the eight samples (see section 2). A total of 17 sessions were conducted in which the different apatite specimens were analyzed for their S isotope composition (see Table A-3 for all SIMS data and Table A-4 for a summary of each session). In each session, besides the sessions during which the homogeneity of large fragments was tested (see section 4.3.3), several fragments of different apatite specimens were repeatedly analyzed in order to test the reproducibility and accuracy of measuring S via SIMS in the respective apatite specimens.

At CMCA, sulfur isotope (^{32}S, ^{33}S and ^{34}S) analyses were performed using a CAMECA IMS1280. Resin mounts were carefully cleaned with detergent, ethanol and distilled water and then coated with 20 nm-thick Au. The sample surface was sputtered over a 15 × 15 μm area with a 10 kV, Gaussian Cs^+ beam with intensity of ~1–3 nA and total impact energy of 20 keV. A normal incidence electron flood gun was used for charge compensation.

Secondary S^- ions were admitted to the double focusing mass spectrometer within a 90 μm entrance slit and focused in the center of a 3000 μm field aperture (x 130 magnification). Energy filtering was applied using a 30 eV band pass with a 5 eV gap toward the high-energy side. The isotopes ^{32}S, ^{33}S and ^{34}S were simultaneously measured with two Faraday Cups using amplifiers with 10^{11} Ω (L1 and H2), and a low-noise ion counting electron multiplier (EM on C). Multicollection detectors operated at a mass resolution of ~4300, which is sufficient to resolve isobaric interferences ^{32}S from $^{31}P^1H$ as well as ^{33}S from $^{32}S^1H$ (Fig. 2). The magnetic field was regulated using NMR control. Each analysis included pre-sputtering over a 20 × 20 μm area during 60s and the automatic centering of the secondary ions in the field aperture. Each analysis then consisted of 30 four-second acquisition periods.

For the isotope homogeneity test of potential reference materials, the stability of the instrument and external precision were monitored using a restricted area (~200 × 100 μm) within a single grain of apatite and by repeating the measurements in this area every five to ten analyses, which targeted other areas of the grain. For accuracy tests, we used apatite samples with a known bulk S isotope composition (see section 4.2) to correct for drift, monitor external standard reproducibility and correct for instrumental mass fractionation. Instrumental drift was corrected via linear functions (see Table A-3).

Sulfur isotope analyses were also performed at the SwissSIMS facility, on a Cameca 1280HR instrument housed at the University of Lausanne. Sulfur isotopes (^{32}S and ^{34}S) were measured as S^- ions, formed by the interaction of a ~ 2–3 nA, $^{133}Cs^+$ primary beam with the sample surface, rastered over a 15 × 15 μm area. The primary beam was accelerated at +10 kV, which resulted in an impact energy of 20 keV on the target surface. The epoxy mounts were cleaned with ethanol, stored in the oven at 50 °C and then coated with a ~ 35 nm Au layer prior to analysis. An electron gun produced low energy electrons that flooded the target area of the Cs + beam in order to avoid charging during the analyses. An entrance slit of 77 μm was used, which focused the secondary ions in the center of a 5000 μm field aperture. The transmission used (MA80) resulted in a field of view of 50 μm. Energy filtering was applied using a 50 eV band pass with a 5 eV gap toward the high-energy side. The ^{32}S isotope was measured through a Faraday cup using amplifiers with 10^{11} Ω (L'2) and simultaneously, the ^{34}S was measured via a low-noise ion counting electron multiplier (EM on H2). Multicollection detector exit slits allowed a mass resolution of ~4300. The magnetic field was regulated using nuclear magnetic resonance (NMR) control. Each analysis included pre-sputtering over a 15 × 15 μm area during 90s and the automatic centering of the secondary ions in the field aperture, followed by 50 cycles of six seconds acquisition.

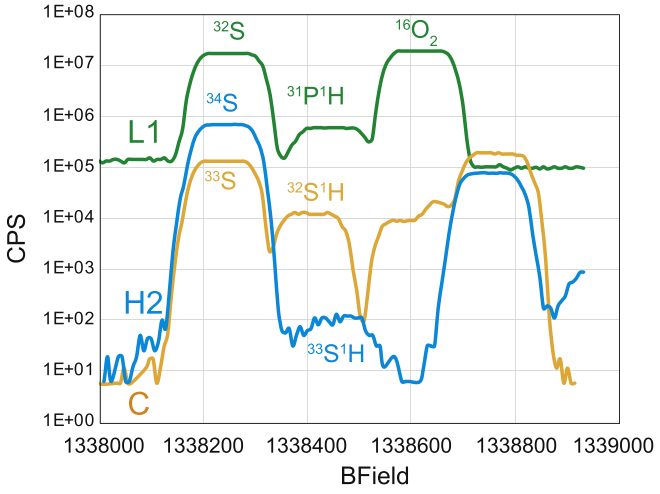

Fig. 2. Magnetic field (B-Field) scan in apatite at a mass resolution of 4300 vs. counts shows the resolution of the interferences on S isotopes. L1, H2, and C refer to the detectors on which the signals were measured.

For the isotope homogeneity test of the potential reference materials, the stability of the instrument and external precision were monitored by repeat analysis of a small area (~200 × 100 μm) within a single grain of Durango (A or B) apatite. This area was analyzed after every four to ten sample analyses. Accuracy tests and drift corrections were similar to those performed at CMCA, besides for one session (see suppl. Material Table A-3) in which a non-linear drift correction was employed.

4. Results

4.1. Major and minor element composition of apatite (EPMA)

Average compositions of the studied apatite determined by EPMA are shown in Table 1. Major element compositions in the analyzed apatite samples range from ~52.9 to 55.9 wt% CaO, ~40.1 to ~42.4 wt % P_2O_5, and from 2.0 to 4.0 wt% F. Chlorine contents are lower and vary from 0.15 to 0.54 wt% between the individual apatite samples, while average FeO and MnO contents are ≤0.05 wt% and ≤ 0.08 wt%, respectively. Hormuz apatite contains the highest Na_2O content (~0.55 wt%), followed by Durango apatites (~0.2 wt%). The other samples contain low (≤ 0.07 wt%) Na_2O contents. The F-rich apatite specimens (SAP1, SAP2, SAP3, Big1) are devoid of OH, according to stoichiometric constraints (Table 1). The highest estimated OH concentration (~1.56 wt% OH) was found in Mdg-1 apatite. The measured SO_3 content in the eight apatite specimens span from 0.04 wt% in Mdg-1 apatite to 0.78 wt % in SAP2. Except for Hormuz apatite, the SiO_2 contents (0.02 to 0.83 wt %) correlate positively with SO_3 concentrations (Fig. 3A). Sulfate and SiO_2 contents, the latter not shown in Fig. 3, increase with decreasing P_2O_5 contents in apatite – again with the exception of Hormuz apatite. These correlations suggest that S and Si are incorporated in apatite at the expense of P, for example via the following substitution (see Pan and Fleet, 2002 for more details on substitutions):

$$2PO_4^{3-} \Leftrightarrow SO_4^{2-} + SiO_4^{4-}$$

In the case of Hormuz apatite, a different substitution mechanism evidently led to the elevated SiO_2 content (Fig. 3). Hormuz apatite contains significant amounts of other trace elements, such up to ~2 wt% of REEs (Faramarzi et al., 2019, Hammerli unpublished data), bringing the total oxides to 100% when combined with our EPMA data (Table 1). It follows that coupled substitutions of REE and SiO_2 for other minor and major elements may explain the relatively high SiO_2 content in Hormuz apatite, despite this being S-poor (see Pan and Fleet, 2002).

4.2. Bulk S isotope analyses

4.2.1. Fluorination

Bulk analysis of SAP1 returned $\delta^{33}S = +6.33 \pm 0.12‰$ (2SE), $\delta^{34}S = +12.26 \pm 0.24‰$ (2SE) and $\delta^{36}S = +23.12 \pm 0.37‰$ (2SE) (Table 2, Table A-1). Sulfur isotope values of sample SAP2 were $\delta^{33}S = +6.38 \pm 0.12‰$ (2SE), $\delta^{34}S = +12.36 \pm 0.24‰$ (2SE) and $\delta^{36}S = +23.37 \pm 0.37‰$ (2SE). Isotope ratios determined for Big1 are $\delta^{33}S = +7.25 \pm 0.12‰$ (2SE), $\delta^{34}S = +14.07 \pm 0.24‰$ (2SE), and $\delta^{36}S = +26.54 \pm 0.37‰$ (2SE). Calculated $\Delta^{33}S$ for the three samples is close to 0 (Table A-1), as suggested in Fig. 4 where $\delta^{33}S$ and $\delta^{34}S$ follow the expected mass dependent fractionation line (Hulston and Thode, 1965).

4.2.2. EA-IRMS

The sulfur isotope value ($\delta^{34}S$) of Durango-A measured by EA-IRMS

Table 1
Average values of EPMA measurements of apatite. Uncertainties are show as the standard deviation of the performed analyses of each sample. The stoichiometries and OH contents are calculated according to Ketcham (2015).

	SAP1		SAP2		SAP3		Big1		Hormuz		Mdg-1		Durango-A		Durango-B	
	(n = 20)		(n = 20)		(n = 20)		(n = 20)		(n = 20)		(n = 25)		(n = 21)		(n = 20)	
	Mean	SD	Mean	SD	Mean	SD	Mean	SD	Mean	SD	Mean	SD	Mean	SD	Mean	SD
CaO (wt%)	55.63	0.19	55.93	0.14	55.69	0.25	55.80	0.25	52.93	0.19	56.13	0.31	54.97	0.25	55.52	0.21
Na_2O	0.07	0.02	0.04	0.02	0.05	0.02	0.05	0.02	0.55	0.03	0.02	0.02	0.22	0.03	0.19	0.03
MnO	0.03	0.01	0.02	0.01	0.01	0.09	0.02	0.01	0.00	0.01	0.08	0.01	0.01	0.01	0.01	0.01
FeO	0.02	0.02	0.01	0.01	0.01	0.01	0.01	0.01	0.04	0.02	0.05	0.02	0.02	0.02	0.03	0.02
MgO	0.01	0.01	0.00	0.00	0.01	0.01	0.01	0.01	0.04	0.01	0.02	0.02	0.01	0.01	0.02	0.01
SO_3	0.55	0.03	0.78	0.04	0.59	0.03	0.75	0.02	0.07	0.01	0.04	0.01	0.31	0.05	0.29	0.02
P_2O_5	40.47	0.53	40.30	0.26	40.55	0.29	40.05	0.24	40.67	0.30	42.38	0.59	41.41	0.21	41.71	0.24
SiO_2	0.62	0.04	0.95	0.04	0.74	0.02	0.83	0.07	0.40	0.02	0.02	0.01	0.33	0.02	0.34	0.02
F	3.89	0.15	3.97	0.30	3.74	0.29	3.86	0.19	3.22	0.14	1.98	0.08	3.47	0.12	3.46	0.30
Cl	0.26	0.01	0.16	0.01	0.15	0.01	0.15	0.01	0.54	0.01	0.07	0.01	0.40	0.05	0.44	0.01
Totals:	101.54	0.59	102.16	0.42	101.53	0.49	101.53	0.40	98.47	0.39	100.79	0.67	101.17	0.35	102.02	0.44
-O(F)	1.64		1.67		1.57		1.62		1.36		0.83		1.46		1.46	
-O(Cl)	0.06		0.04		0.03		0.03		0.12		0.02		0.09		0.10	
Corr. Tot.	99.84		100.45		99.93		99.87		96.99		99.94		99.62		100.46	
+est. OH wt%									0.13		1.56		0.05		0.07	
Net Corr. Tot.	99.84		100.45		99.93		99.87		97.12		101.50		99.67		100.53	
APFU	Mean		Mean		Mean		Mean		Mean		Mean		Mean		Mean	
Ca	10.079		10.059		10.052		10.100		9.820		10.015		9.937		9.957	
Na	0.024		0.013		0.016		0.018		0.183		0.006		0.073		0.061	
Mn	0.004		0.003		0.001		0.003		0.001		0.011		0.001		0.001	
Fe	0.003		0.001		0.001		0.001		0.006		0.007		0.003		0.004	
Mg	0.001		0.000		0.002		0.002		0.011		0.005		0.003		0.004	
S	0.069		0.098		0.075		0.095		0.009		0.005		0.040		0.037	
∑	*10.180*		10.174		*10.148*		*10.219*		*10.030*		*10.050*		*10.057*		*10.065*	
P	5.793		5.727		5.784		5.728		5.961		5.975		5.915		5.911	
Si	0.105		0.159		0.125		0.140		0.070		0.003		0.056		0.057	
∑	*5.898*		5.886		*5.909*		*5.868*		*6.031*		*5.978*		*5.972*		*5.968*	
F	2.078		2.107		1.991		2.061		1.765		1.043		1.854		1.832	
Cl	0.073		0.046		0.043		0.044		0.157		0.020		0.114		0.124	
OH									0.078		0.937		0.032		0.043	

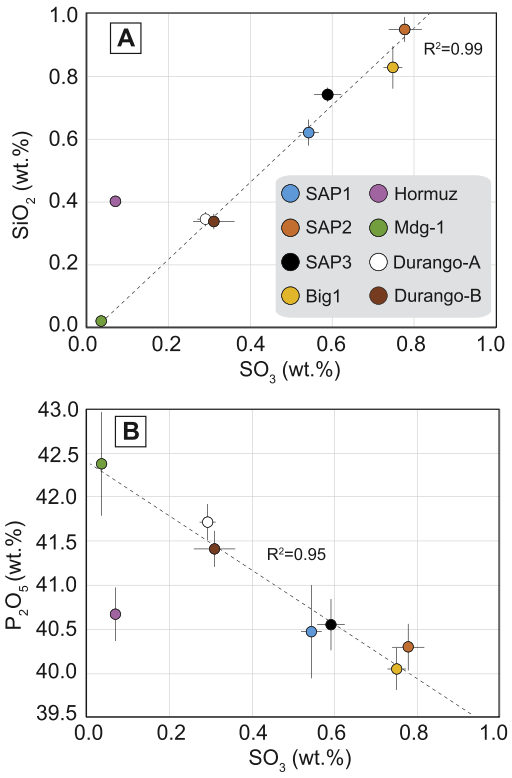

Fig. 3. A) Average SiO_2 (wt%) vs. SO_3 (wt%) content of the analyzed apatites. The SiO_2 and SO_3 contents of the apatites are positively and linearly correlated. The exception is Hormuz apatite which does not plot on the linear regression ($R^2 = 0.99$). B) SO_3 and P_2O_5 are negatively correlated but also form a linear regression ($R^2 = 0.95$). Hormuz apatite plots outside the linear correlation (see text for more details), likely due to a significant amount of incorporated REE.

is −1.06 ± 0.80‰ (2SD), which is slightly higher than the $\delta^{34}S$ value obtained by the same method for the Durango-B sample (−1.31 ± 0.80‰, 2SD) (Table 2).

4.2.3. MC-ICP-MS

The measured S isotope composition of apatite samples SAP1, SAP2, SAP3, Big1, Durango-B, and Mdg-1 are shown in Table 2. The $\delta^{34}S$ values for SAP1, SAP2, SAP3, and Big1 range from around +12.3 to around +13.7‰, while Durango-B retuned a $\delta^{34}S$ value of −1.44 ± 0.60‰ (2SD). Hormuz apatite contains a $\delta^{34}S$ value of +25.78 ± 0.60‰ and analysis of Mdg-1 apatite returned +1.42 ± 0.60‰. $\delta^{33}S$ numbers for SAP1, SAP2, SAP3, and Big1 range from 6 to 7‰ (Table 2). Durango-B returned a $\delta^{33}S$ value of −0.88 ± 0.30‰ and Hormuz apatite and Mdg-1 apatite contain $\delta^{33}S$ values of +13.19 ± 0.30‰ and 0.64 ± 0.30‰, respectively. The S isotope ratios determined by MC-ICP-MS follow the MDF line (Fig. 4); these results reflect the accuracy of data produced by the MC-ICP-MS method.

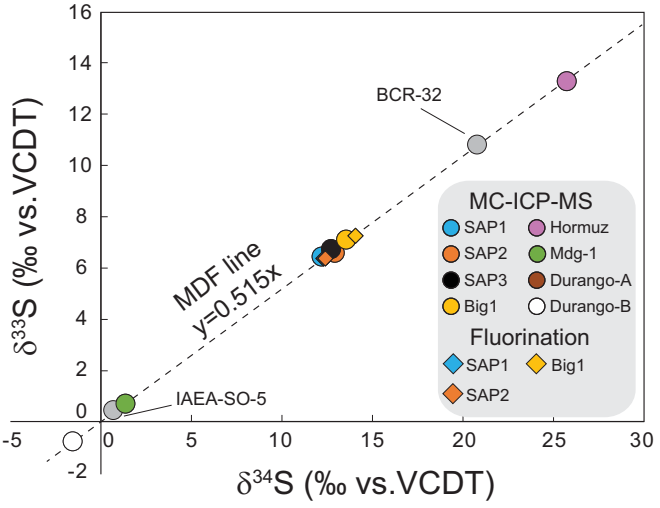

Fig. 4. Plot of $\delta^{34}S$ vs. $\delta^{33}S$ in of the apatite samples analyzed by the fluorination method (diamond symbols) and MC-ICP-MS (round symbols). Note that all samples, including the BCR-32 and IAEA-SO-5 standards fall on the expected MDF line (Hulston and Thode, 1965).

4.3. S isotope analyses by SIMS

4.3.1. S concentration in apatite vs. SIMS counts

The eight apatite samples were measured in a total of seventeen analytical sessions (Tables 3–5) and all analyses can be found in the supplementary Table A-3. The relative S isotope count rates between the sample with the highest (SAP2) and lowest (Mdg-1) S concentration differ by a factor of ~20. SIMS S count rates on mass 32 (^{32}S), shown as yield (cps/beam intensity), are in excellent agreement with the SO_3 contents determined by EPMA over a large range of S contents of apatite (Fig. 5).

4.3.2. Sulfur isotope homogeneity

We tested the individual apatite samples for their isotope homogeneity via SIMS measurements along transects across the embedded grains. In the case of euhedral crystals (Big1, Durango-A, Durango-B), we conducted transects along the different crystallographic axes (see sections 4.3.3 and Fig. 6). For specimens for which the crystallographic orientation could not be determined optically (SAP1, SAP3, Mdg-1), analyses were performed along transects of randomly orientated large

Table 2
Mean S concentrations in the studied samples and S isotope ratios (‰ vs. VCDT) of bulk measurements and simple mean values of all SIMS measurements shown in Fig. 8. *For the samples, for which different methods were employed to determine bulk grain values, the mean bulk values are the error-weighted means at 95% confidence intervals.

	EPMA	Fluorination	MC-ICP-MS	EA-IRMS	Mean Bulk*	Mean SIMS	Fluorination	MC-ICP-MS	Mean Bulk*	SIMS
	S (μg/g) (2SD)	$\delta^{34}S$ (‰) (2SE)	$\delta^{34}S$ (‰) (2SD)	$\delta^{34}S$ (‰) (2SD)	$\delta^{34}S$ (‰)	$\delta^{34}S$ (‰) (2SD)	$\delta^{33}S$ (‰) (2SE)	$\delta^{33}S$ (‰) (2SD)	$\delta^{33}S$ (‰)	$\delta^{33}S$ (‰) (2SD)
SAP1	2202 ± 240	12.26 ± 0.24	12.30 ± 0.60		12.27 ± 0.22	12.52 ± 0.89	6.33 ± 0.12	6.33 ± 0.30	6.33 ± 0.11	6.45 ± 1.12
SAP2	3123 ± 320	12.36 ± 0.24	13.05 ± 0.60		12.46 ± 0.22	13.79 ± 0.53	6.38 ± 0.12	6.53 ± 0.30	6.40 ± 0.11	7.04 ± 0.66
SAP3	2363 ± 240		12.85 ± 0.60		12.85 ± 0.60	13.54 ± 0.97		6.65 ± 0.30	6.65 ± 0.30	7.17 ± 1.06
Big1	3003 ± 160	14.07 ± 0.24	13.68 ± 0.60		14.02 ± 0.22	13.58 ± 0.70	7.25 ± 0.12	7.03 ± 0.30	7.22 ± 0.11	6.85 ± 0.71
Hormuz	280 ± 80		25.78 ± 0.60		25.78 ± 0.60	25.48 ± 3.37		13.19 ± 0.30	13.19 ± 0.30	12.78 ± 2.12
Mdg-1	160 ± 80		1.42 ± 0.60		1.42 ± 0.60	−0.50 ± 2.46		0.64 ± 0.30	0.64 ± 0.30	−0.59 ± 1.99
Durango-A	1241 ± 400			−1.06 ± 0.80	−1.06 ± 0.80	−1.57 ± 0.85				−0.82 ± 1.07
Durango-B	1161 ± 160		−1.44 ± 0.60	−1.31 ± 0.80	−1.39 ± 0.48	−1.60 ± 1.24		−0.88 ± 0.30	−0.88 ± 0.30	−0.54 ± 1.11

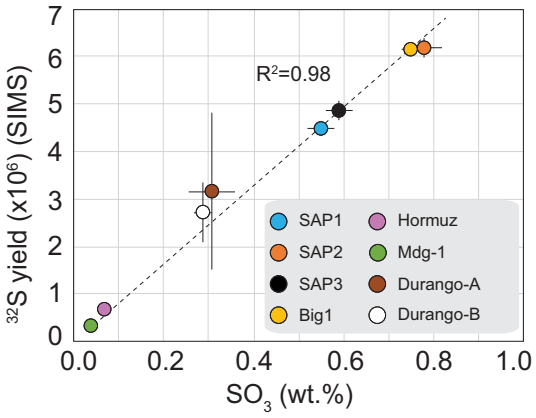

Fig. 5. SO_3 (wt%) contents determined by EPMA of the studied samples vs. yield of mass 32 by SIMS. Error bars are 2SD.

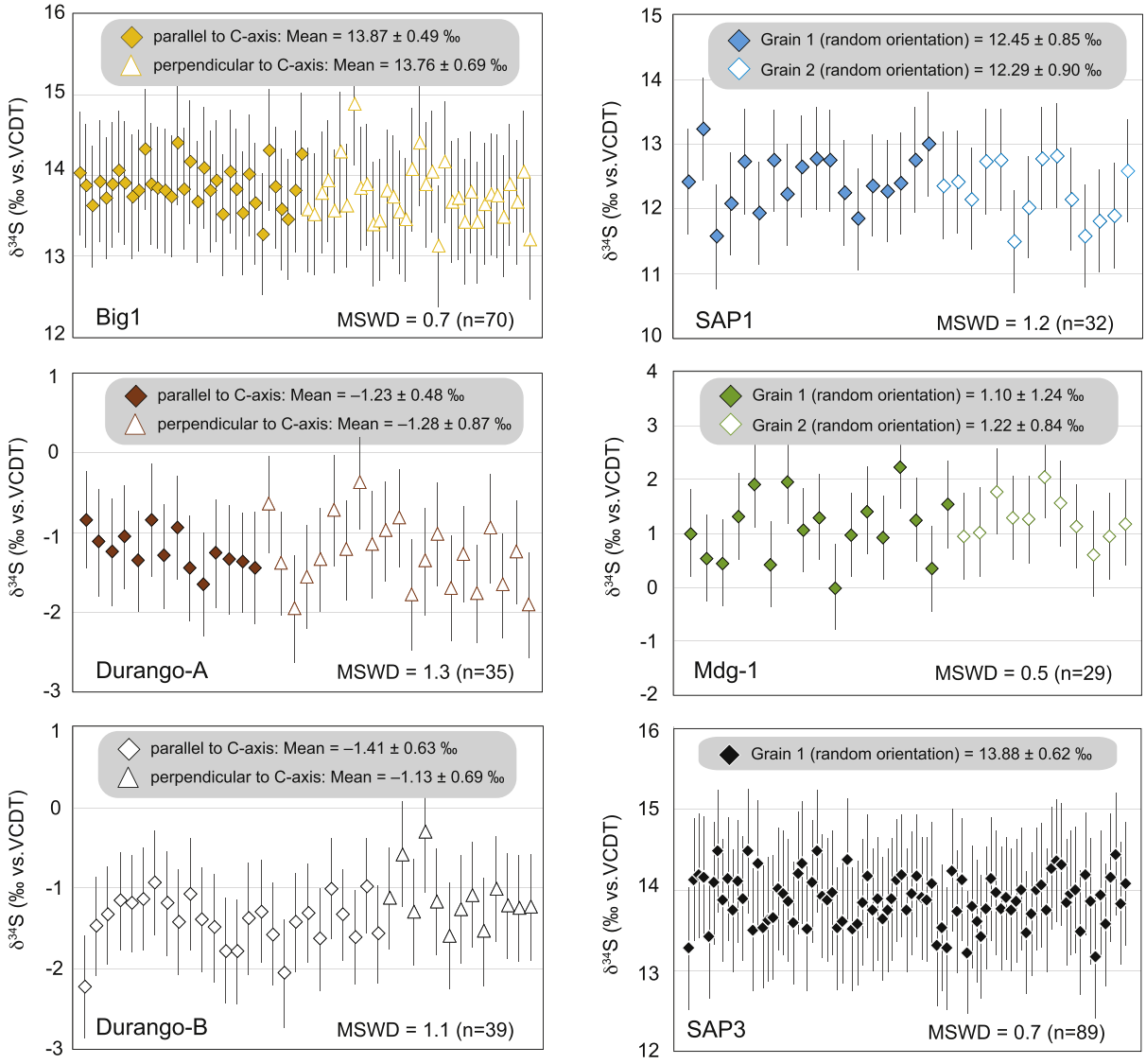

Fig. 6. SIMS S isotope analyses along different crystallographic axes (parallel and perpendicular to the c-axis) in Big1, Durango-A, Durango-B and transects across large, randomly orientated fragments of SAP1 and Mdg-1 apatite. All analyses within the respective fragment are within their analytical uncertainties, which is the combined internal and external error at 95% CI. Repeated analyses of a small area within each grain were used for drift correction and standardization with bulk values taken from Table 2.

crystal fragments. Transects across all analyzed samples yielded isotopically homogeneous results, also evident from low (≤ 1.3) MSWD values (Fig. 6). Except for the sessions where transects and/or large fragments were analyzed, throughout each analytical session, the analyses were performed in several different fragments of each sample (see section 4.3.4). Additionally, more than 20 individual fragments of specimen SAP1, SAP3, and Big1 were analyzed to further test their S isotope homogeneity. The results showed that all analyses were within the analytical uncertainty (see also Fig. 8), confirming the results of the transects.

4.3.3. Crystal orientation effect on instrumental mass fractionation

Crystallographic orientations can have significant impacts on the instrumental mass fractionation of SIMS analyses (e.g., Taylor et al., 2012). In order to test if the crystallographic orientation of apatite affected the instrumental mass fractionation of S isotopes, we analyzed three samples (Durango-A, Durango-B, and Big1), along and perpendicular to their crystallographic c-axis (Fig. 6). These transects also served to assess the isotope homogeneity of the studied samples (see section 4.3.2). A small area (~200 × 100 μm) of the respective grain was repeatedly analyzed to monitor instrumental drift during the analyses and was used accordingly for drift correction. Analyses of this small area were also used to to calculate the $\delta^{34}S$ value of the individual analysis (Fig. 6) via the weighted mean bulk values of the respective apatite specimen (Table 2). Our results provide no evidence for any crystallographic influence on the instrumental mass fractionation of S isotopes for the different samples. The means of the differently oriented grains are indistinguishable for each respective sample, with mean square of weighted deviates (MSWD) close to 1 (Fig. 6). This is a similar finding as reported by Bruand et al. (2019) who did not observe a crystallographic impact on SIMS oxygen isotope analyses in apatite.

4.3.4. Precision and accuracy

The internal precision of single spot S isotope analyses via SIMS strongly correlates with counting statistics, which are directly related to the S concentration of the sample. Our data show that internal uncertainties (standard error of the mean cycle measurements during a single analysis) of around ±0.2‰ (2SE) for the $^{34}S/^{32}S$ isotope ratio ($\delta^{34}S$) and ~ 0.5‰ for $\delta^{33}S$ can be achieved (Fig. 7). The external reproducibility (standard deviation of the analyses of the reference material during an analytical sessions) depends on the homogeneity of the material and on external analytical factors, such as instrumental drift, which in some cases needs to be corrected for. The external reproducibility within individual sessions varies from around ±0.3‰ to

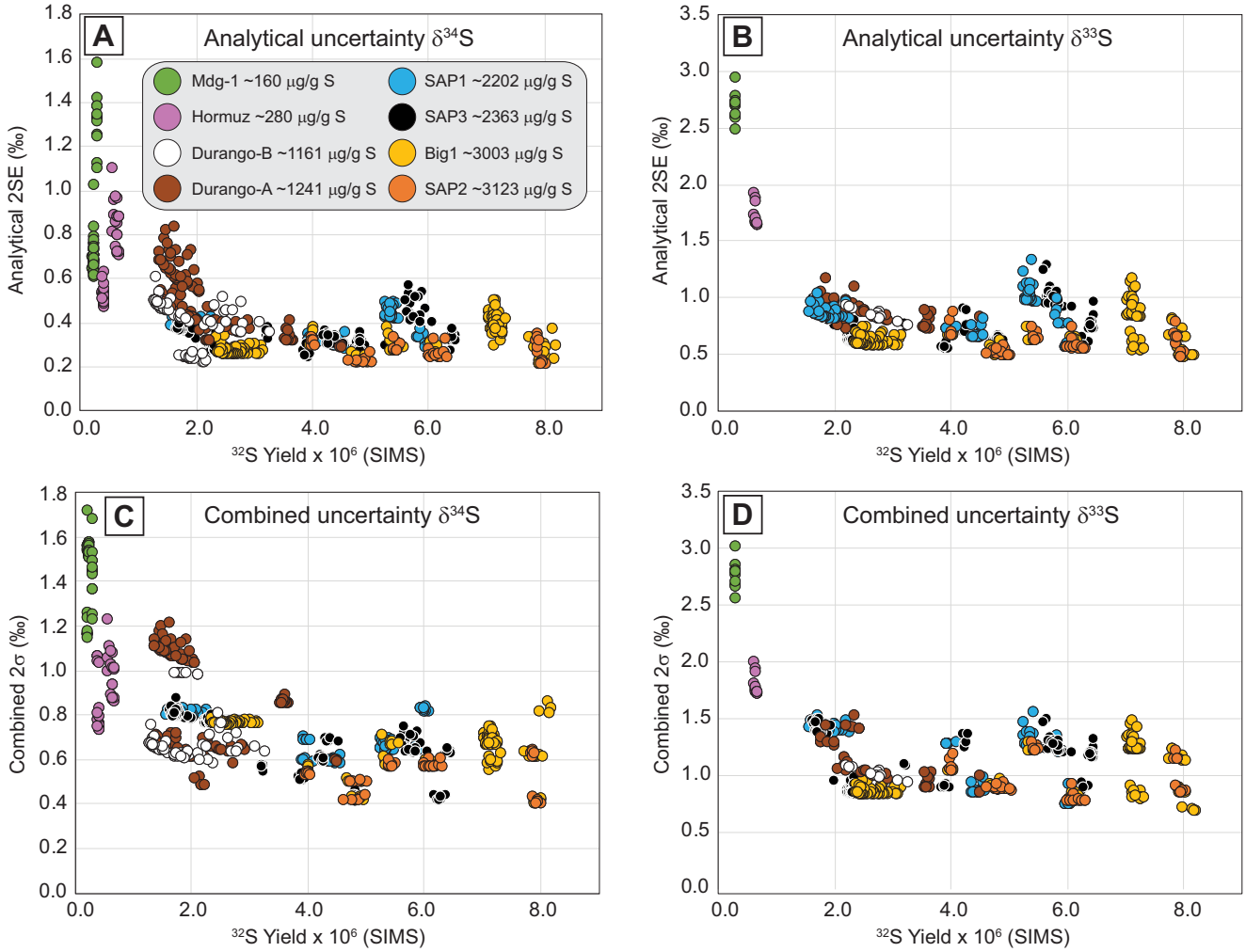

Fig. 7. A) & B) Analytical uncertainties of $\delta^{34}S$ vs. ^{32}S yields (count rates normalized by beam intensities) and $\delta^{33}S$ vs. ^{32}S yields by SIMS. Note the clear correlation of lower uncertainties with increasing yields, which broadly reflect the S contents of the samples. The minimum analytical precision (2SE) achieved for $\delta^{34}S$ is around ±0.2 ‰ and ± 0.5 ‰ for $\delta^{33}S$. C) & D) Combined (propagated) uncertainties include the single spot analytical precision added with the repeatability of the reference material used for standardization in quadrature. The lowest propagated errors (2σ) achieved for $\delta^{34}S$ are around ±0.4 ‰ (D) and around ±0.7 ‰ for $\delta^{33}S$. Note that the smaller spread in the combined uncertainty for some of the samples is a result of multiple sessions in which the repeatability of the reference material is different.

Table 3
Repeatability (2SD) of reference material (RM) during each analytical session.

			$\delta^{33}S$ (‰ vs. VCDT)		$\delta^{34}S$ (‰ vs. VCDT)	
Session	n	RM	Ref. Value	2SD	Ref. Value	2SD
04.05.17	36	Big1	7.22	0.58	14.02	0.72
17.10.17	19	SAP1	6.33	1.11	12.27	0.71
15.03.18	54	Big1	7.22	0.79	14.02	0.49
01.06.18	17	SAP1	6.33	0.68	12.27	0.34
25.06.18	18	Durango-A			−1.06	0.54
26.06.18	22	SAP2	6.40	0.47	12.46	0.63
31.08.19	16	SAP1	6.33	0.79	12.27	0.45
31.08.19	25	SAP1	6.33	0.71	12.27	0.45
31.08.19	8	SAP1	6.33	0.72	12.27	0.35
29.02.20	17	Durango-A			−1.06	0.62
01.03.20	14	Durango-B	−0.88	1.05	−1.39	0.53
01.07.20	16	SAP1	6.33	0.57	12.27	0.47
01.07.20	12	SAP3	6.65	0.52	12.85	0.51
09.01.18	10	Durango-A			−1.06	0.95
10.01.18	22	Durango-A			−1.06	0.57
29.05.18	27	Durango-B			−1.39	0.44

±1.0‰ (2SD) for the $^{34}S/^{32}S$ isotope ratio (Table 3). This means that single spot uncertainty for S isotope quantification, which is the combined internal uncertainty with the external reproducibility of the primary apatite, summed in quadrature, is commonly controlled by the repeatability (external reproducibility) of the reference material (see Fig. 7). Single spot uncertainties as low as ~0.4‰ (for $\delta^{34}S$) and ~ 0.7‰ (for $\delta^{33}S$) can be achieved in samples with ≥0.3 wt% SO_3 (~1200 μg/g S), which translate to a yield (cps/beam intensity) of ≥2 × 10^6 for ^{32}S (Fig. 7).

Based on transects of large mineral grains together with analyses of >20 individual grains of the samples SAP1, SAP3, and Big1, our results suggest that apatite specimens SAP1, SAP3, Big1, Durango-A, Durango-B, and Mdg-1 have an internally consistent S isotope composition within the respective analytical session. By using the weighted mean bulk S isotope ratios of apatite SAP1, SAP3, Big1, Durango-A, Durango-B, and SAP2 as reference values (Table 2) to standardize S isotope analyses of "unknowns" (i.e., any of the other seven apatite specimens tested in this study), we were able to assess which apatite specimens were the most reliable for reproducing the bulk S isotope values of the "unknowns". Our results, reported as simple means, show that by using SAP1, SAP3, Big1, Durango-A, and Durango-B apatite as reference materials, the bulk S isotope values of the "unknowns" can be reproduced within uncertainty (Fig. 8, Table 4). The exception is SAP2, whose bulk isotope values could not be reproduced using any of the above apatite specimens as reference material, resulting in a discrepancy of >1‰ between SIMS and bulk analyses (Fig. 8 and Table 4). It is therefore possible that the SAP2 apatite aliquot used for bulk analyses had a slightly different S isotope composition than the material analyzed via the SIMS method. This might also explain the discrepancy in the S isotope ratios produced by the fluorination ($\delta^{34}S$ = 12.34‰) and MC-ICP-MS methods ($\delta^{34}S$ = 13.05‰). A further test for the reliability of the different reference materials (RMs) are the MSWD values of the combined analyses (Fig. 8). The MSWD values for analyses of SAP1, Big1, and Durango-A are ≤1.7. This, in combination with the average values of the "unknowns" (which are for these three specimens in agreement with bulk values), further support the consistency of the method and attest to the homogeneity of the RMs. The elevated MSWD of apatite specimen SAP3 (2.1) might suggest that a slight isotope heterogeneity outside the analytical uncertainty exists. We therefore do not recommend SAP3 as a primary RM (see section 5.2). In contrast, despite the elevated MSWD of Durango-B apatite, which is mostly a result of the session in which SAP3 was employed as a RM, the bulk S isotope values of the "unknowns" (Table 4) can be reproduced within the analytical uncertainty. Thus, we consider Durango-B as a reliable RM for SIMS S isotope analyses (see section 5.2).

Despite the similarity of the isotope ratios of the two Durango apatite specimens investigated in this study, it is possible that crystal to crystal S isotope variations in apatite from this locality exist, as has been observed for oxygen isotopes (Sun et al., 2016). This is possibly also manifested by slightly higher bulk S isotope ratio (0.34 ± 0.04 ‰ (2SD) $\delta^{34}S$) reported by Economos et al. (2017). If these higher S isotope values were used as RM, the $\delta^{34}S$ SIMS values of the unknowns (i.e., the other apatite specimens in this study) would be significant higher.

The apatite specimens with the lowest S concentrations of ~160 and ~ 320 μg/g (Mdg-1 and Hormuz) show larger variations between different analytical sessions. Mean $\delta^{34}S$ values for Mdg-1 measured in two SIMS sessions range from +0.6‰ to −1.2‰. The latter session (−1.2‰, Table 4 and Fig. 8) in which several individual Mdg-1 grains were analyzed showed a poor repeatability of ±2.2 (2SD) ‰. This potentially points toward a certain degree of S isotope heterogeneity in the Mdg-1 crystal, which was not recorded in the transect analyses. The average $\delta^{34}S$ values of SIMS analyses is −0.6 ± 1.99 (2SD) ‰, (n = 20, MSWD = 3.4). The measured bulk value is slightly heavier and returned a $\delta^{34}S$ value of +1.4 ± 0.6‰ (Table 2). Hormuz apatite contains the highest S isotope ratios. Average $\delta^{34}S$ values of SIMS analyses with different RMs are between +23.3 and + 26.5‰ (Fig. 8, Table 4), with an overall mean of +25.5 ± 3.4 (2SD) ‰ (n = 37) (Table 2). Despite the relatively poor reproducibility, the average $\delta^{34}S$ value agrees well with the bulk value of +25.8‰ ± 0.60 (2SD) ‰ (Table 2). The large scatter in the S isotope composition of Hormuz apatite might be the result of S isotope heterogeneity within the crystal, which is also reflected by the high MSWD value of 14.

A comparison of mean $\delta^{34}S$ values determined via SIMS and via bulk $\delta^{34}S$ numbers (Fig. 8, Table 2), shows an excellent overall agreement in values between the different techniques (Fig. 9a) (Note: there is discrepancy between SIMS and bulk values in one sample, SAP2; see Fig. 8). This agreement in measured values across a range of different apatite samples supports the accuracy of the SIMS method. In addition to the excellent agreement of the $^{34}S/^{32}S$ ratio between individual SIMS sessions and bulk analyses, our results also show that $\delta^{33}S$ values of apatite measured by SIMS and by the different bulk techniques are equivalent within their analytical uncertainty and repeatability. Exceptions to this are the SIMS analyses of SAP2, which is likely due to sample heterogeneity (see above), and analyses from one session in which Big1 was analyzed with SAP2 as the RM (Tables 2, 5, Fig. 9b and supplementary Figs. A-1 & A-2). Fig. 10 shows that the $\delta^{33}S$ and $\delta^{34}S$ values (shown as the simple means) determined by SIMS follow the MDF line. However, samples with low S contents show relatively large uncertainties for their $^{33}S/^{32}S$ ratio ($\delta^{33}S$) (Table 5), which is also reflected when $\Delta^{33}S$ is plotted against $\delta^{34}S$ (Fig. 10b). By increasing the primary beam intensity or the counting time during the analyses of low S apatite, the precision of the $\delta^{33}S$ measurements could be improved.

4.3.5. *Matrix bias in ion microprobe apatite measurements*

Instrumental mass fractionation by SIMS is inherently linked to the composition of the target material, as well as to the specific analytical conditions under which the samples are measured (e.g., Eiler et al., 1997; Kozdon et al., 2010). Except for Mdg-1 apatite, which contains a significant OH component (~1.6 wt% OH), all minerals tested in this study contain high F concentrations and belong to the F-rich apatite variety (SAP1, SAP2, SAP3, Big1, Durango, Hormuz). Hormuz is the only tested apatite, which contains elevated Cl (~0.6 wt%). We do not observe any matrix bias for S isotope SIMS analyses outside the analytical uncertainties. Sulfur isotope values in apatite normalized to different apatite reference material of different compositions returned indistinguishable S isotope ratios in homogeneous samples (Figs. 8, A-1, A-2, Table 4). Based on our data we infer that the analytical precision is controlled by the S content of apatite (Fig. 7). While the studied apatite

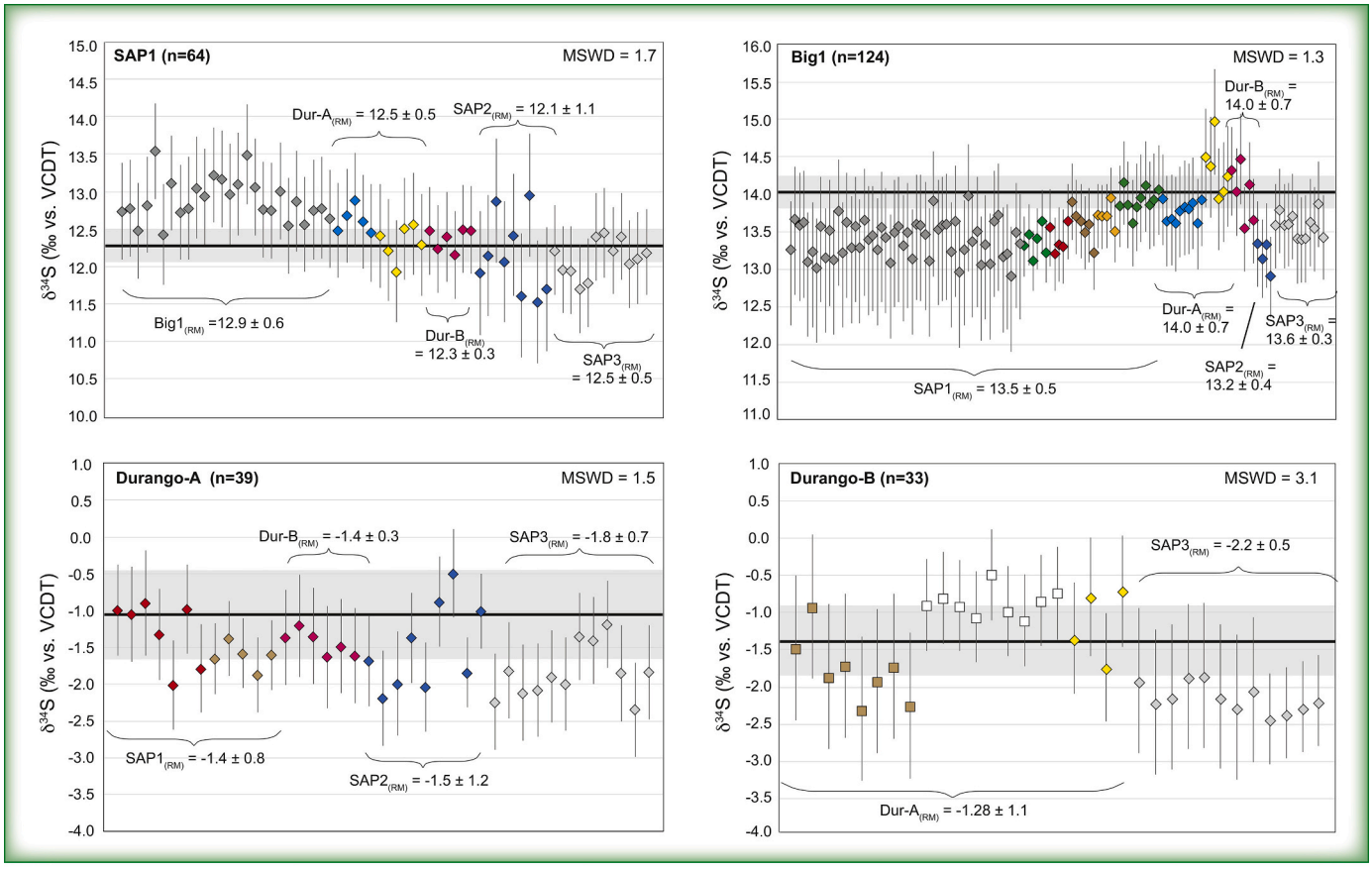

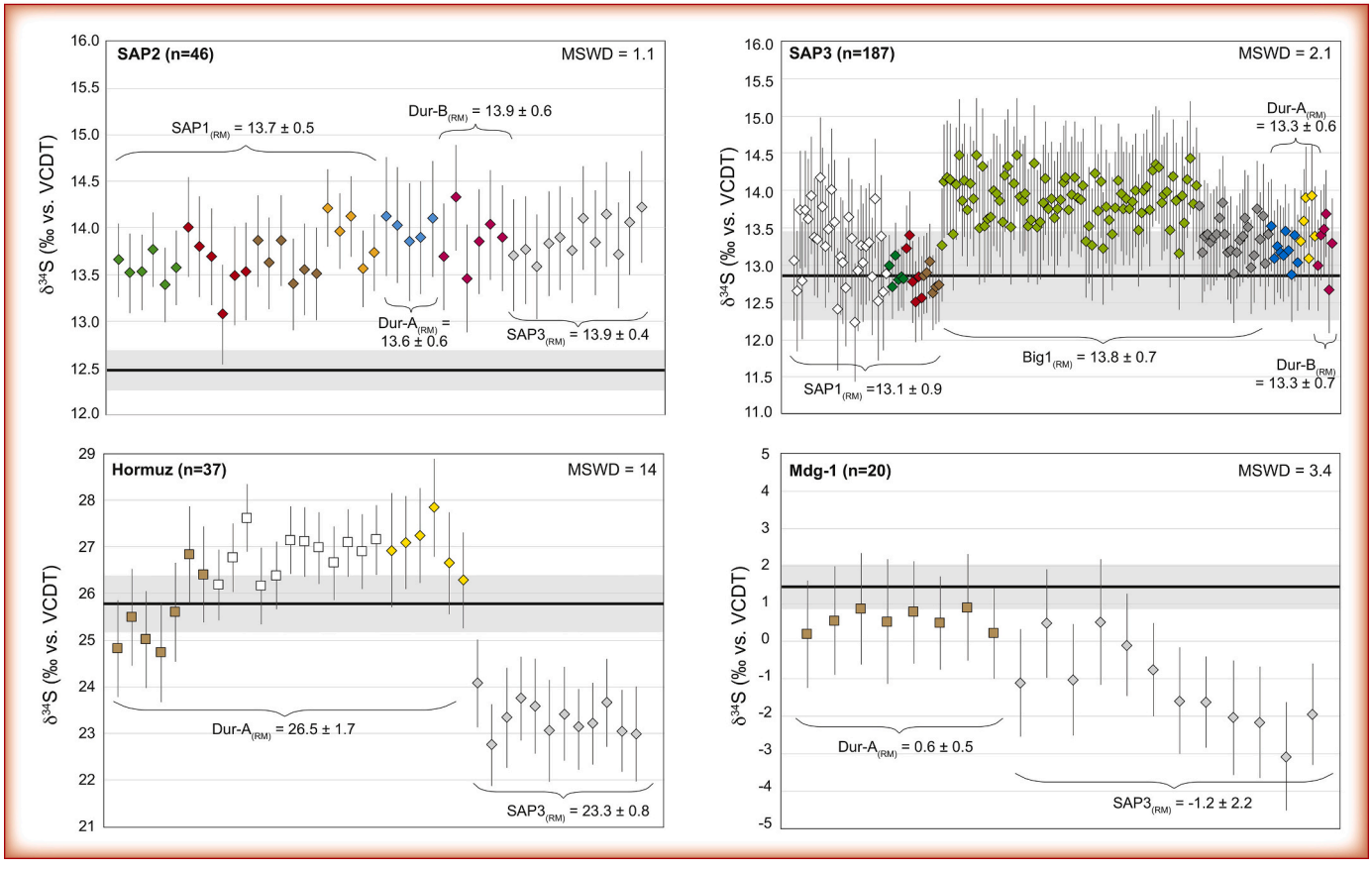

(caption on next page)

Fig. 8. Reproducibility of S isotope measurements in the eight apatite samples, as assessed by individual SIMS analyses (each color indicates a different analytical session see also Fig. A-3 and Table A-4), where the measured $^{34}S/^{32}S$ ratios are normalized to the bulk $\delta^{34}S$ values (see Table 2) of different apatite specimens (e.g., $Big1_{(RM)}$) with the corresponding mean. Data presented in the green outline (top box) are apatite specimens whose bulk S isotope values can be reproduced via SIMS analyses, while apatite specimens in the red box show discrepancy between SIMS measurements and bulk values. All data points include 2SD uncertainties, which combine in-run (measured) uncertainties and the standard deviation of the repeated analyses of the reference material during the respective session, summed in quadrature. Diamond symbols show analyses conducted at the CMCA, UWA, and square symbols show analyses carried out at University of Lausanne. For each analytical session several grains of the respective sample were analyzed (see also table A-4). The solid black lines represent bulk values and grey areas show the 95% CI (see Table 2). (For interpretation of the references to color in this figure legend, the reader is referred to the web version of this article.)

Table 4
Mean $\delta^{34}S$ (‰ vs. VCDT) values of the eight apatite specimens standardized via different reference materials (see also Fig. 8) with their respective bulk values taken from Table 2. For mean values of each individual session see Table A-4. Uncertainties are at the 95% CI.

	SAP1	Big1	Dur-A	Dur-B	SAP2	SAP3	Hormuz	Mdg-1
	$\delta^{34}S$ (‰)	$\delta^{34}S$ (‰)	$\delta^{34}S$ (‰)	$\delta^{34}S$ (‰)	$\delta^{34}S$ (‰)	$\delta^{34}S$ (‰)	$\delta^{34}S$ (‰)	$\delta^{34}S$ (‰)
Bulk value	12.27 ± 0.22	14.02 ± 0.22	−1.06 ± 0.80	−1.39 ± 0.48	12.46 ± 0.22	12.85 ± 0.60	25.78 ± 0.60	1.42 ± 0.60
Reference Material								
SAP1		13.49 ± 0.59	−1.43 ± 0.76		13.67 ± 0.52	13.11 ± 0.91		
Big1	12.89 ± 0.56					13.77 ± 0.91		
Durango-A	12.46 ± 0.50	13.98 ± 0.74		−1.28 ± 1.09	13.60 ± 0.64	13.34 ± 0.59	26.52 ± 1.66	0.56 ± 0.54
Durango-B	12.38 ± 0.29	14.02 ± 0.73	−1.44 ± 0.33		13.88 ± 0.59	13.26 ± 0.73		
SAP2	12.13 ± 1.05	13.18 ± 0.41	−1.50 ± 1.19					
SAP3	12.12 ± 0.48	13.58 ± 0.31	−1.84 ± 0.72	−2.16 ± 0.38	13.82 ± 0.41		23.30 ± 0.76	−1.21 ± 2.26

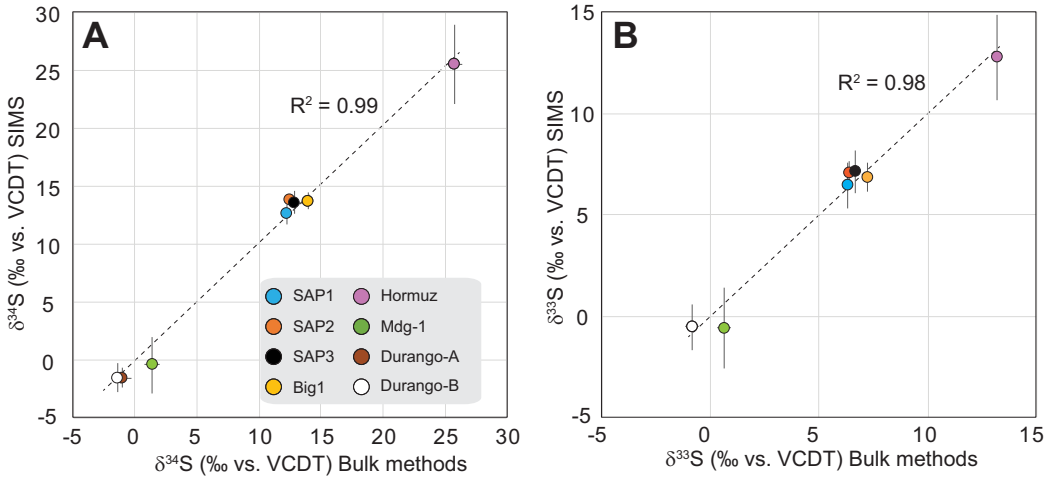

Fig. 9. A) Mean $\delta^{34}S$ values determined by SIMS vs. mean $\delta^{34}S$ values determined by bulk methods (data taken from Table 2). B) Mean $\delta^{33}S$ values determined by SIMS vs. mean $\delta^{33}S$ values determined by bulk methods (data taken from Table 2). Uncertainties are shown at the 95% CI. Regression lines are forced through the origin.

Table 5
Mean $\delta^{33}S$ (‰ vs. VCDT) values of the eight apatite specimens standardized via different reference materials with their respective bulk values taken from Table 2. For mean values of each individual session see Table A-5. Uncertainties are at the 95% CI.

	SAP1	Big1	Dur-A	Dur-B	SAP2	SAP3	Hormuz	Mdg-1
	$\delta^{33}S$ (‰)	$\delta^{33}S$ (‰)	$\delta^{33}S$ (‰)	$\delta^{33}S$ (‰)	$\delta^{33}S$ (‰)	$\delta^{33}S$ (‰)	$\delta^{33}S$ (‰)	$\delta^{33}S$ (‰)
Bulk value	6.33 ± 0.11	7.22 ± 0.11		−0.88 ± 0.30	6.40 ± 0.11	6.65 ± 0.30	13.19 ± 0.30	0.64 ± 0.30
Reference Material								
SAP1		6.86 ± 0.74	−0.77 ± 0.98		7.09 ± 0.68	7.10 ± 1.42		
Big1	6.77 ± 0.90					7.25 ± 0.76		
Durango-B	5.92 ± 1.14	6.77 ± 0.67	−0.77 ± 0.63		6.80 ± 0.60	6.30 ± 0.67		
SAP2	5.81 ± 0.57	6.43 ± 0.40	−1.37 ± 0.99					
SAP3	6.49 ± 0.59	6.95 ± 0.44	−0.50 ± 0.83	−0.54 ± 1.11	7.06 ± 0.59		12.78 ± 2.12	−0.59 ± 1.99

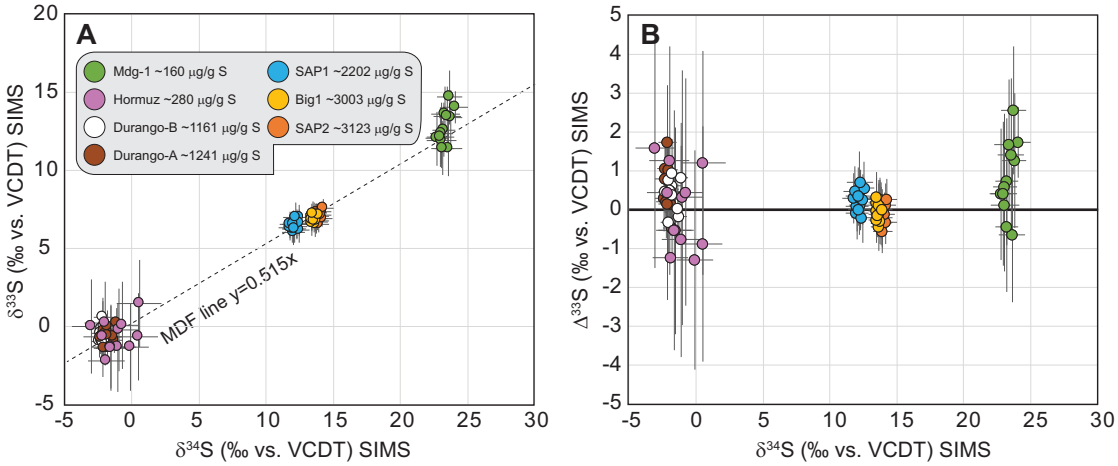

Fig. 10. A) $\delta^{33}S$ (VCDT) vs. $\delta^{34}S$ (VCDT) and B) $\Delta^{33}S$ (VCDT) vs. $\delta^{34}S$ (VCDT), normalized of the bulk value of sample SAP3 from session 1.7.2020. Error bars for $\delta^{34}S$ and $\delta^{33}S$ are the overall uncertainty (2SD) based on propagating the analytical uncertainty with the repeatability for the relevant reference material during each analytical session. Uncertainty calculations for $\Delta^{33}S$ were performed following the method outlined in LaFlamme et al. (2016).

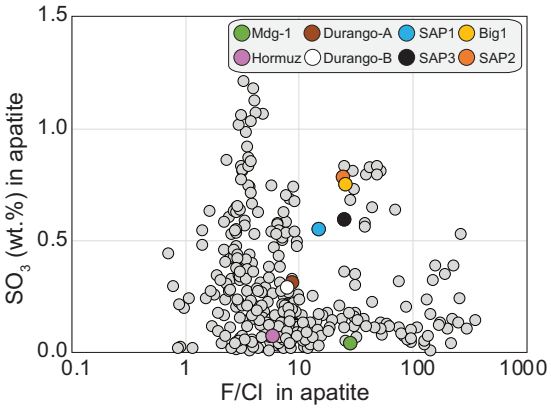

Fig. 11. F/Cl (wt%) ratios in S-bearing apatite grains (data from Chu et al., 2009; Cao et al., 2011; Mao et al., 2016) compared to the apatite samples characterized in this study.

specimens contain F/Cl ratios typical for S-bearing apatite (Fig. 11), we emphasize that no Cl or OH apatite end-member has been tested thus far for potential mass bias effects on the instrument mass fractionation for S isotope quantification.

5. Discussion

5.1. Multiple S isotope analyses in apatite by SIMS

We report multiple S isotope analyses in apatite on a bulk and sub-mineral scale. Our study shows that in situ SIMS S isotope analyses can be conducted in apatite with a range of S concentrations from a few hundred µg/g S to thousands of µg/g S. Furthermore, S isotope analyses in two different SIMS facilities with different analytical set-ups (see section 3.3.4) show that S isotope values in different apatite specimens can be reproduced to within 1‰ $\delta^{34}S$, supporting the robustness of the characterized reference materials. A key strength of in situ SIMS S isotope analyses is the 10–20 µm spatial resolution. This offers unique insights into the geochemical changes of a system, which can be recorded in (apatite) minerals. While S is preferentially incorporated as S^{6+} in apatite in oxidized environments where apatite with elevated S contents are formed (e.g., Parat et al., 2011a, 2011b), quantification of S isotope compositions in apatite with low S concentrations, as shown in Hormuz and Mdg-1 apatite in this study, may also permit the characterisation of S isotope signatures in apatite from reduced environments where S partitioning between fluids and apatite are typically low (e.g., Parat et al., 2011a, 2011b; Konecke et al., 2017; Sadove et al., 2019). Based on our data we further propose that MIF $\Delta^{33}S$ anomalies (>1‰) can be detected in apatite that contains S concentrations >1000 µg/g by using SAP1, Big1, or Durango-B as a primary reference material to determine the $^{33}S/^{32}S$ ratio in apatite samples.

Our data show that the S isotope signature of apatite can range over ≥25‰ $\delta^{34}S$. This means that this very common mineral can record the sulfur isotope fingerprints of inherently different systems and environments (Fig. 1). The stability of S-bearing mineral phases (i.e., sulfides and sulfates) traditionally used for in-situ S isotope analyses is commonly restricted to certain pressure-temperature and redox conditions; in contrast, apatite is stable under a large range of igneous, hydrothermal, and metamorphic conditions (Fig. 12). Additionally, our study shows, for the first time, that $\delta^{33}S$ isotope values in apatite can be accurately and precisely measured via the SIMS methodology. This unlocks new opportunities to detect and trace S isotope anomalies formed in specific geological environments and at a certain time in Earth evolution (e.g., Farquhar et al., 2000). Given that apatite commonly incorporates several hundreds of µg/g S in its crystal lattice (Fig. 12), promising new avenues emerge to better understand S sources and cycles via S isotope measurements in apatite. For example, S isotope analyses by SIMS in apatite might be useful to track S sources throughout the evolution of mineralized systems, from their sulfide-free pre-mineralization stages through to mineralization and post mineralization events. Similarly, S (re-)cycling in convergent settings can be tracked, especially in sulfide-barren metamorphic and igneous rocks, where

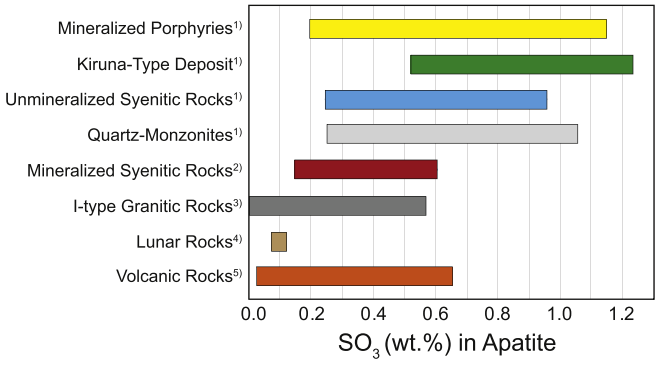

Fig. 12. Compilation of SO_3 (wt%) contents in apatite in a variety of systems. Note that accurate SIMS analyses can be achieved in samples with ≥0.1 wt% SO_3. 1)Mao et al. (2016); 2)Cao et al. (2011); 3)Chu et al. (2009); 4)Brounce et al. (2019); 5)Peng et al. (1997)

Table 6
Recommended S isotope (‰ vs. VCDT) reference values of apatite SAP1, Big1, Durango-A, and Durango-B for in situ S isotope analyses in apatite by SIMS. Recommended values for SAP1 and Big1 are the weighted means of fluorination analyses and MC-ICP-MS measurements. The S isotope value of Durango-A was determined by EA-IRMS and the $\delta^{34}S$ value of Durango-B is the weighted mean of MC-ICP-MS and EA-IRMS analysis. The $\delta^{33}S$ value of Durango-B was determined by MC-ICP-MS. All uncertainties are at the 95% CI.

	S content	Recommended	Recommended
	(μg/g)	$\delta^{34}S$ (‰)	$\delta^{33}S$ (‰)
SAP1	2202 ± 240	12.27 ± 0.22	6.33 ± 0.11
Big1	3003 ± 160	14.02 ± 0.22	7.22 ± 0.11
Durango-A	1241 ± 400	−1.06 ± 0.80	
Durango-B	1161 ± 160	−1.39 ± 0.48	−0.88 ± 0.30

apatite is the only S-bearing mineral phase.

We show that in situ SIMS S isotope analyses in apatite is a robust technique with no effects from crystallographic orientations (see also Economos et al., 2017). This is an important finding for accurate S isotope analysis in detrital apatite grains, whose crystallographic orientation is often challenging to determine due to their worn and abraded textures. Finally, in order to further test and confirm the absence of matrix effects on the instrumental fractionation beyond the tested apatite compositions (Fig. 11), future examinations for potential matrix bias in OH-and Cl-end-member apatite should be undertaken.

5.2. Recommended S isotope reference values

The different bulk methods employed to characterize the apatite specimens produced S isotope values that are within 1‰ $\delta^{34}S$ with each other (see section 2 and Table 2). Based on bulk and SIMS analyses, we propose Big1 (~3000 μg/g S), SAP1 (~2200 μg/g S), Durango-A (~1240 μg/g S) and Durango-B (~1160 μg/g S) as suitable reference materials for SIMS analyses. We suggest using the weighted mean bulk isotope ratios for standardization, which are +12.27 ± 0.22 (2σ) ‰ $\delta^{34}S$ and 6.33 ± 0.11 (2σ) ‰ $\delta^{33}S$ for SAP1, +14.02 ± 0.22 (2σ) ‰ $\delta^{34}S$ and 7.22 ± 0.11 (2σ) ‰ $\delta^{33}S$ for Big1, −1.39 ± 0.48 (2σ) and −0.88 ± 0.30 (2σ) ‰ $\delta^{33}S$ for Durango-B, and −1.06 ± 0.80 (2σ) ‰ $\delta^{34}S$ for Durango-A (Table 6). We recommend using at least two RMs for the analysis of natural samples, especially when a wide range of S concentrations and isotope ratios is expected. Using RMs with similar S concentrations as the unknown helps with analytical protocols that use an electron multiplier.

5.3. Geological significance of different isotope ratios of analyzed samples

Finally, we will briefly discuss the S isotope values of the analyzed apatite in their geological context. First, we focus on those apatite specimens for which the location of their formation is well known: the Durango apatite and Hormuz apatite. Those two samples also contain the two most extreme S isotope values of the analyzed samples in this study. Durango apatite comes from the Cerro de Mercado Iron Oxide Apatite (IOA) deposit, which is located in the City of Durango, Mexico. The Cerro de Mercado IOA deposit is situated within Chupaderos Caldera Complex, which belongs to a large Oligocene (~31.5 Ma) rhyolitic volcanic system (McDowell et al., 2005). It is hypothesized that the iron ore formed through multiple subaerial volcanic processes, fed by an iron-rich magma containing significant amounts of halogens, CO_2, and water. In this setting, apatite is thought to have formed in a magmatic-hydrothermal system where it crystallized in cavities formed by fugitive halogen-rich vapor phases, which led to the redistribution and concentration of ore metal (Lyons, 1988). Conversely, Barton and Johnson (1996) argued for an evaporitic control on the ligand availability for metal transport, opposed to the above model, which envisages phase separation of the ascending magma for the production of a halogen-rich gas phase capable of ore metal transportation and eventual deposition. Our S isotope data from the Cerro de Mercado IOA deposit show no evidence for the involvement of S sourced from evaporitic horizons. Sulfur sourced from evaporites typically contains a much heavier $\delta^{34}S$ isotope fingerprint (> 10‰ $\delta^{34}S$ and see Hormuz case study below) than the S isotope signature we observed in Durango apatite (~ −1.4‰). This means that the sulfur isotope values in Durango apatite support a magmatic-hydrothermal model for ore genesis at the Cerro de Mercado Iron Oxide Apatite deposit.

In contrast, apatite from the same study as Hurford et al. (1984), collected from a fine-grained red iron oxide outcrop from Hormuz Island, situated in the Persian Gulf, Iran, contains a strikingly heavy S isotope signature of ~ +25.8 ± 0.9 (2SD) $\delta^{34}S$ ‰ (bulk analyses) and +25.5 ± 3.4 (2SD) $\delta^{34}S$ ‰ (SIMS). Hormuz Island, which hosts IOA mineralization, belongs to a salt-diapir, which at ~558 Ma delivered rhyolitic and rhyodacitic rocks, together with gypsum, to the surface (e.g., Faramarzi et al., 2019 and references therein). The heavy S isotope signature in Hormuz apatite supports a model of magmatic fluid interaction with evaporite horizons (Peters et al., 2020) for at least the formation of the apatite in the IOA ore.

The exact localities of the apatite samples from Madagascar (Mdg-1, SAP1, SAP2, SAP3, and Big1) are not known. The sample termed "Mdg-1" apatite comes from Milanoa of the Vohémar district in northeastern Madagascar according to information obtained from the mineral collection of the Natural History Museum Bern. The region around Milanoa hosts multiple mineralized systems including pegmatites (pers. comm. Guido Schreurs). While the exact location or host rock of Mgd-1 is unknown, mantle-like S isotope values obtained from bulk analyses (+1.4‰ $\delta^{34}S$) and in situ SIMS measurements (~ −0.6‰ $\delta^{34}S$) suggest that no evaporitic S sources were involved in the formation of the mineralizing fluids. This is in contrast to the apatite samples (SAP1, SAP2, SAP2 and Big1). While their location is not known, we speculate that these samples come from southern Madagascar and possibly from the Beraketa shear zone – a province known for the occurrence of large apatite minerals (Morteani et al., 2013). Previous studies have shown that in this region, silico-carbonatitic melt of crustal origin digested evaporitic lithologies, resulting in a heavy S isotope signature (up to ~ +18‰ $\delta^{34}S$) in pyrite of pegmatites (Morteani et al., 2013). The elevated S isotope values +12 to +14‰ $\delta^{34}S$ in SAP1, SAP2, SAP3, and Big1 suggest an input of heavy S from seawater or evaporitic material. Hence, S isotope signatures in apatite might be a useful approach to trace the origins of apatite gemstones whose origins are unknown or debated, especially if they have unusual S isotope signatures.

6. Conclusions

Our newly characterized apatite reference materials (SAP1, Big1, Durango-A, and Durango-B) allow for routine high spatial resolution SIMS S isotope quantification in apatite in a large range of geological environments. This finding makes the already versatile mineral apatite an even more useful and important mineral to trace fluid and magma sources. SIMS S isotope analyses in apatite can be combined with a wide range of other in situ techniques to extract valuable information for igneous, metamorphic, and hydrothermal processes, such as for melt sources via in-situ Sm-Nd isotope analyses (e.g., Hammerli et al., 2018) or fluid compositions and sources via quantification of the volatile inventory of individual apatite grains (e.g., Kusebauch et al., 2015). Reference material is available for distribution to SIMS laboratories from johannes.haemmerli@geo.unibe.ch or nicolas.greber@geo.unibe.ch.

Declaration of Competing Interest

The authors declare that they have no known competing financial interests or personal relationships that could have appeared to influence the work reported in this paper.

Acknowledgements

We thank Richard Stern and an anonymous reviewer for their constructive comments and suggestions, which helped to improve this paper significantly. We also thank the editor Balz Kamber for handling this paper. This work was supported by Swiss National Science Foundation grants PZ00P2_180095, 181172 and 182007 to JH, NDG and US. The authors acknowledge the facilities, and the scientific and technical assistance of the Australian Microscopy & Microanalysis Research Facility at the Centre for Microscopy, Characterisation & Analysis, The University of Western Australia, a facility funded by the University, State and Commonwealth Governments. The Neptune MC-ICP-MS at the University of Bern was acquired with funds from the National Centre for Competence in Research PlanetS supported by the Swiss National Science Foundation (SNSF). Pierre Lanari is thanked for help with EPMA measurements. This is contribution 1576 from the ARC Centre of Excellence for Core to Crust Fluid Systems. Prof. Beda Hofmann from the NMB and Patrick Boehnke are thanked for providing apatite material for this study.

Appendix A. Supplementary data

Supplementary data to this article can be found online at https://doi.org/10.1016/j.chemgeo.2021.120242.

References

Alt, J.C., Shanks, W.C., Jackson, M.C., 1993. Cycling of sulfur in subduction zones: the geochemistry of sulfur in the Mariana Island Arc and back-arc trough. Earth Planet. Sci. Lett. 119, 477–494. https://doi.org/10.1016/0012-821X(93)90057-G.

Barton, M.D., Johnson, D.A., 1996. Evaporitic-source model for igneous-related Fe oxide–(REE-Cu-Au-U) mineralization. Geology 24, 259–262.

Benmore, R.A., Coleman, M.L., McArthur, J.M., 1983. Origin of sedimentary francolite from its sulphur and carbon isotope composition. Nature 302, 516–518. https://doi.org/10.1038/302516a0.

Benning, L.G., Seward, T.M., 1996. Hydrosulphide complexing of Au (I) in hydrothermal solutions from 150–400°C and 500–1500 bar. Geochim. Cosmochim. Acta 60, 1849–1871. https://doi.org/10.1016/0016-7037(96)00061-0.

Boehnke, P., Bell, E.A., Stephan, T., Trappitsch, R., Keller, C.B., Pardo, O.S., Davis, A.M., Harrison, T.M., Pellin, M.J., 2018. Potassic, high-silica Hadean crust. Proc. Natl. Acad. Sci. 115, 6353–6356. https://doi.org/10.1073/pnas.1720880115.

Boyce, J.W., Liu, Y., Rossman, G.R., Guan, Y., Eiler, J.M., Stolper, E.M., Taylor, L.A., 2010. Lunar apatite with terrestrial volatile abundances. Nature 466, 466–469. https://doi.org/10.1038/nature09274.

Brand, W.A., Coplen, T.B., Vogl, J., Rosner, M., Prohaska, T., 2014. Assessment of international reference materials for isotope-ratio analysis (IUPAC Technical Report). Pure Appl. Chem. 86, 425–467. https://doi.org/10.1515/pac-2013-1023.

Brounce, M., Boyce, J., McCubbin, F.M., Humphreys, J., Reppart, J., Stolper, E., Eiler, J., 2019. The oxidation state of sulfur in lunar apatite. Am. Mineral. 104, 307–312. https://doi.org/10.2138/am-2019-6804.

Bruand, E., Storey, C., Fowler, M., Heilimo, E., 2019. Oxygen isotopes in titanite and apatite, and their potential for crustal evolution research. Geochim. Cosmochim. Acta 255, 144–162. https://doi.org/10.1016/j.gca.2019.04.002.

Cabral, R.A., Jackson, M.G., Rose-Koga, E.F., Koga, K.T., Whitehouse, M.J., Antonelli, M. A., Farquhar, J., Day, J.M.D., Hauri, E.H., 2013. Anomalous sulphur isotopes in plume lavas reveal deep mantle storage of Archaean crust. Nature 496, 490–493. https://doi.org/10.1038/nature12020.

Canfield, D.E., 2004. The evolution of the Earth surface sulfur reservoir. Am. J. Sci. 304, 839–861.

Chaussidon, M., Lorand, J.-P., 1990. Sulphur isotope composition of orogenic spinel lherzolite massifs from Ariege (North-Eastern Pyrenees, France): an ion microprobe study. Geochim. Cosmochim. Acta 54, 2835–2846. https://doi.org/10.1016/0016-7037(90)90018-G.

Cao, M., Li, G., Qin, K., Seitmuratova, E.Y., Liu, Y., 2011. Major and trace element characteristics of apatites in granitoids from central Kazakhstan: implications for petrogenesis and mineralization: major and trace element of apatites. Resour. Geol. 62, 63–83. https://doi.org/10.1111/j.1751-3928.2011.00180.x.

Chaussidon, M., Albarede, F., Sheppard, S.M.F., 1989. Sulphur isotope variations in the mantle from ion microprobe analyses of micro-sulphide inclusions. Earth Planet. Sci. Lett. 92, 144–156.

Chu, M.-F., Wang, K.-L., Griffin, W.L., Chung, S.-L., O'Reilly, S.Y., Pearson, N.J., Iizuka, Y., 2009. Apatite composition: tracing petrogenetic processes in transhimalayan granitoids. J. Petrol. 50, 1829–1855. https://doi.org/10.1093/petrology/egp054.

Delavault, H., Chauvel, C., Thomassot, E., Devey, C.W., Dazas, B., 2016. Sulfur and lead isotopic evidence of relic Archean sediments in the Pitcairn mantle plume. Proc. Natl. Acad. Sci. 113, 12952–12956. https://doi.org/10.1073/pnas.1523805113.

Ding, T., et al., 2001. Calibrated sulfur isotope abundance ratios of three IAEA sulfur isotope reference materials and V-CDT with a reassessment of the atomic weight of sulfur. Geochim. Cosmochim. Acta 65, 2433–2437.

Economos, R., Boehnke, P., Burgisser, A., 2017. Sulfur isotopic zoning in apatite crystals: a new record of dynamic sulfur behavior in magmas. Geochim. Cosmochim. Acta 215, 387–403. https://doi.org/10.1016/j.gca.2017.08.015.

Eiler, J.M., Graham, C., Valley, J.W., 1997. SIMS analysis of oxygen isotopes: matrix effects in complex minerals and glasses. Chem. Geol. 138, 221–244.

Evans, K.A., 2012. The redox budget of subduction zones. Earth-Sci. Rev. 113, 11–32. https://doi.org/10.1016/j.earscirev.2012.03.003.

Evans, K.A., Tomkins, A.G., Cliff, J., Fiorentini, M.L., 2014. Insights into subduction zone sulfur recycling from isotopic analysis of eclogite-hosted sulfides. Chem. Geol. 365, 1–19. https://doi.org/10.1016/j.chemgeo.2013.11.026.

Faramarzi, N.S., Jamshidibadr, M., Heuss-Assbichler, S., Borg, G., 2019. Mineral chemistry and fluid inclusion composition as petrogenetic tracers of iron oxide-apatite ores from Hormuz Island, Iran. J. Afr. Earth Sci. 155, 90–108. https://doi.org/10.1016/j.jafrearsci.2019.03.018.

Farquhar, J., Wing, B.A., 2003. Multiple sulfur isotopes and the evolution of the atmosphere. Earth Planet. Sci. Lett. 213, 1–13. https://doi.org/10.1016/S0012-821X(03)00296-6.

Farquhar, J., Bao, H., Thiemens, M., 2000. Atmospheric Influence of Earth's Earliest Sulfur Cycle. Science 289, 756–758. https://doi.org/10.1126/science.289.5480.756.

Farquhar, J., Wing, B.A., McKeegan, K.D., Harris, J.W., Cartigny, P., Thiemens, M.H., 2002. Mass-independent sulfur of inclusions in diamond and sulfur recycling on early earth. Science 298, 2369–2372. https://doi.org/10.1126/science.1078617.

Farquhar, J., Wu, N., Canfield, D.E., Oduro, H., 2010. Connections between sulfur cycle evolution, sulfur isotopes, sediments, and base metal sulfide deposits. Econ. Geol. 105, 509–533.

Giacometti, F., Evans, K.A., Rebay, G., Cliff, J., Tomkins, A.G., Rossetti, P., Vaggelli, G., Adams, D.T., 2014. Sulfur isotope evolution in sulfide ores from Western Alps: Assessing the influence of subduction-related metamorphism. Geochem. Geophys. Geosyst. 15, 3808–3829. https://doi.org/10.1002/2014GC005459.

Goedert, J., Fourel, F., Amiot, R., Simon, L., Lécuyer, C., 2016. High-precision 34S/32S measurements in vertebrate bioapatites using purge-and-trap elemental analyser/isotope ratio mass spectrometry technology. Rapid Commun. Mass Spectrom. 30, 2002–2008. https://doi.org/10.1002/rcm.7690.

Hammerli, J., Kemp, A.I.S., Barrett, N., Wing, B.A., Roberts, M., Arculus, R.J., Boivin, P., Nude, P.M., Rankenburg, K., 2017. Sulfur isotope signatures in the lower crust: a SIMS study on S-rich scapolite of granulites. Chem. Geol. 454, 54–66. https://doi.org/10.1016/j.chemgeo.2017.02.016.

Hammerli, J., Kemp, A.I.S., Shimura, T., Vervoort, J.D., Dunkley, D.J., 2018. Generation of I-type granitic rocks by melting of heterogeneous lower crust. Geology 46, 907–910. https://doi.org/10.1130/G45119.1.

Harmon, R.S., Hoefs, J., Wedepohl, K.H., 1987. Stable isotope (O, H, S) relationships in Tertiary basalts and their mantle xenoliths from the Northern Hessian depression. W.-Germany. Contrib. Mineral. Petrol. 95, 350–369.

Hattori, K.H., Keith, J.D., 2001. Contribution of mafic melt to porphyry copper mineralization: evidence from Mount Pinatubo, Philippines, and Bingham Canyon, Utah, USA. Mineral. Deposita 36, 799–806. https://doi.org/10.1007/s001260100209.

de Hoog, J.C.M., Taylor, B.E., van Bergen, M.J., 2001. Sulfur isotope systematics of basaltic lavas from Indonesia: implications for the sulfur cycle in subduction zones. Earth Planet. Sci. Lett. 189, 237–252. https://doi.org/10.1016/S0012-821X(01)00355-7.

Hulston, J.R., Thode, H.G., 1965. Variations in the S 33, S 34, and S 36 contents of meteorites and their relation to chemical and nuclear effects. J. Geophys. Res. 70, 3475–3484. https://doi.org/10.1029/JZ070i014p03475.

Hurford, A.J., Grunau, H.R., Stöcklin, J., 1984. Fission track dating of an apatite crystal from Hormuz Island, Iran. J. Pet. Geol. 7, 365–380. https://doi.org/10.1111/j.1747-5457.1984.tb00883.x.

Ionov, D.A., Hoefs, J., Wedepohl, K.H., Wiechert, U., 1992. Content and isotopic composition of sulphur in ultramafic xenoliths from Central Asia. Earth Planet. Sci. Lett. 111, 269–286. https://doi.org/10.1016/0012-821X(92)90184-W.

Ketcham, R.A., 2015. Technical note: Calculation of stoichiometry from EMP data for apatite and other phases with mixing on monovalent anion sites. Am. Mineral. 100, 1620–1623. https://doi.org/10.2138/am-2015-5171.

Kiba, T., Takagi, T., Yoshimura, Y., Kishi, I., 1955. Tin (II)-strong phosphoric acid. A new reagent for the determination of sulfate by reduction to hydrogen sulfide. Bull. Chem. Soc. Jpn. 28, 641–644.

Kita, N.T., Huberty, J.M., Kozdon, R., Beard, B.L., Valley, J.W., 2011. High-precision SIMS oxygen, sulfur and iron stable isotope analyses of geological materials: accuracy, surface topography and crystal orientation. Surf. Interface Anal. 43, 427–431. https://doi.org/10.1002/sia.3424.

Konecke, B.A., Fiege, A., Simon, A.C., Parat, F., Stechern, A., 2017. Co-variability of S6+, S4+, and S2− in apatite as a function of oxidation state: Implications for a new oxybarometer. Am. Mineral. 102, 548–557. https://doi.org/10.2138/am-2017-5907.

Konecke, B.A., Fiege, A., Simon, A.C., Linsler, S., Holtz, F., 2019. An experimental calibration of a sulfur-in-apatite oxybarometer for mafic systems. Geochim. Cosmochim. Acta 265, 242–258. https://doi.org/10.1016/j.gca.2019.08.044.

Kozdon, R., Kita, N.T., Huberty, J.M., Fournelle, J.H., Johnson, C.A., Valley, J.W., 2010. In situ sulfur isotope analysis of sulfide minerals by SIMS: precision and accuracy, with application to thermometry of ~3.5Ga Pilbara cherts. Chem. Geol. 275, 243–253. https://doi.org/10.1016/j.chemgeo.2010.05.015.

Kusebauch, C., John, T., Whitehouse, M.J., Engvik, A.K., 2015. Apatite as probe for the halogen composition of metamorphic fluids (Bamble Sector, SE Norway). Contrib. Mineral. Petrol. 170 https://doi.org/10.1007/s00410-015-1188-6.

Labidi, J., Cartigny, P., Birck, J.L., Assayag, N., Bourrand, J.J., 2012. Determination of multiple sulfur isotopes in glasses: a reappraisal of the MORB δ34S. Chem. Geol. 334, 189–198. https://doi.org/10.1016/j.chemgeo.2012.10.028.

Labidi, J., Cartigny, P., Moreira, M., 2013. Non-chondritic sulphur isotope composition of the terrestrial mantle. Nature 501, 208–211. https://doi.org/10.1038/nature12490.

Labidi, J., Shahar, A., Le Losq, C., Hillgren, V.J., Mysen, B.O., Farquhar, J., 2016. Experimentally determined sulfur isotope fractionation between metal and silicate and implications for planetary differentiation. Geochim. Cosmochim. Acta 175, 181–194. https://doi.org/10.1016/j.gca.2015.12.001.

LaFlamme, C., Martin, L., Jeon, H., Reddy, S.M., Selvaraja, V., Caruso, S., Bui, T.H., Roberts, M.P., Voute, F., Hagemann, S., Wacey, D., Littman, S., Wing, B., Fiorentini, M., Kilburn, M.R., 2016. In situ multiple sulfur isotope analysis by SIMS of pyrite, chalcopyrite, pyrrhotite, and pentlandite to refine magmatic ore genetic models. Chem. Geol. 444, 1–15. https://doi.org/10.1016/j.chemgeo.2016.09.032.

Lyons, J.I., 1988. Volcanogenic iron oxide deposits, Cerro de Mercado and vicinity. Durango. Econ. Geol. 83, 1886–1906. https://doi.org/10.2113/gsecongeo.83.8.1886.

Magnall, J.M., Gleeson, S.A., Stern, R.A., Newton, R.J., Poulton, S.W., Paradis, S., 2016. Open system sulphate reduction in a diagenetic environment – Isotopic analysis of barite (δ34S and δ18O) and pyrite (δ34S) from the Tom and Jason late Devonian Zn–Pb–Ba deposits, Selwyn Basin, Canada. Geochim. Cosmochim. Acta 180, 146–163. https://doi.org/10.1016/j.gca.2016.02.015.

Mao, M., Rukhlov, A.S., Rowins, S.M., Spence, J., Coogan, L.A., 2016. Apatite trace element compositions: a robust new tool for mineral exploration. Econ. Geol. 111, 1187–1222. https://doi.org/10.2113/econgeo.111.5.1187.

Marin-Carbonne, J., Busigny, V., Miot, J., Rollion-Bard, C., Muller, E., Drabon, N., Jacob, D., Pont, S., Robyr, M., Bontognali, T.R.R., François, C., Reynaud, S., Van Zuilen, M., Philippot, P., 2020. In Situ Fe and S isotope analyses in pyrite from the 3.2 Ga Mendon Formation (Barberton Greenstone Belt, South Africa): evidence for early microbial iron reduction. Geobiology 18, 306–325. https://doi.org/10.1111/gbi.12385.

Marini, L., Moretti, R., Accornero, M., 2011. Sulfur isotopes in magmatic-hydrothermal systems, melts, and magmas. Rev. Mineral. Geochem. 73, 423–492. https://doi.org/10.2138/rmg.2011.73.14.

McCubbin, F.M., Jones, R.H., 2015. Extraterrestrial Apatite: Planetary Geochemistry to Astrobiology. Elements 11, 183–188. https://doi.org/10.2113/gselements.11.3.183.

McDowell, F.W., McIntosh, W.C., Farley, K.A., 2005. A precise 40Ar–39Ar reference age for the Durango apatite (U–Th)/He and fission-track dating standard. Chem. Geol. 214, 249–263. https://doi.org/10.1016/j.chemgeo.2004.10.002.

Morteani, G., Kostitsyn, Y.A., Gilg, H.A., Preinfalk, C., Razakamanana, T., 2013. Geochemistry of phlogopite, diopside, calcite, anhydrite and apatite pegmatites and syenites of southern Madagascar: evidence for crustal silicocarbonatitic (CSC) melt formation in a Panafrican collisional tectonic setting. Int. J. Earth Sci. 102, 627–645. https://doi.org/10.1007/s00531-012-0832-x.

Ono, S., Wing, B., Johnston, D., Farquhar, J., Rumble, D., 2006. Mass-dependent fractionation of quadruple stable sulfur isotope system as a new tracer of sulfur biogeochemical cycles. Geochim. Cosmochim. Acta 70, 2238–2252.

Pan, Y., Fleet, M.E., 2002. Compositions of the apatite-group minerals: substitution mechanisms and controlling factors. Rev. Mineral. Geochem. 48, 13–49. https://doi.org/10.2138/rmg.2002.48.2.

Parat, F., Holtz, F., Streck, M.J., 2011b. Sulfur-bearing Magmatic Accessory Minerals. Rev. Mineral. Geochem. 73, 285–314. https://doi.org/10.2138/rmg.2011.73.10.

Parat, Fleurice, Holtz, F., Klügel, A., 2011a. S-rich apatite-hosted glass inclusions in xenoliths from La Palma: constraints on the volatile partitioning in evolved alkaline magmas. Contrib. Mineral. Petrol. 162, 463–478. https://doi.org/10.1007/s00410-011-0606-7.

Peng, G., Luhr, J.F., McGee, J.J., 1997. Factors controlling sulfur concentrations in volcanic apatite. Am. Mineral. 82, 1210–1224. https://doi.org/10.2138/am-1997-11-1217.

Peters, S.T.M., Alibabaie, N., Pack, A., McKibbin, S.J., Raeisi, D., Nayebi, N., Torab, F., Ireland, T., Lehmann, B., 2020. Triple oxygen isotope variations in magnetite from iron-oxide deposits, Central Iran, record magmatic fluid interaction with evaporite and carbonate host rocks. Geology 48, 211–215. https://doi.org/10.1130/G46981.1.

Sadove, G., Konecke, B.A., Fiege, A., Simon, A.C., 2019. Structurally bound S2−, S1−, S4+, S6+ in terrestrial apatite: the redox evolution of hydrothermal fluids at the Phillips mine, New York, USA. Ore Geol. Rev. 107, 1084–1096. https://doi.org/10.1016/j.oregeorev.2019.03.033.

Sakai, H., Marais, D.J.D., Ueda, A., Moore, J.G., 1984. Concentrations and isotope ratios of carbon, nitrogen and sulfur in ocean-floor basalts. Geochim. Cosmochim. Acta 48, 2433–2441. https://doi.org/10.1016/0016-7037(84)90295-3.

Schneider, A., 1970. The sulfur isotope composition of basaltic rocks. Contrib. Mineral. Petrol. 25, 95–124. https://doi.org/10.1007/BF00389779.

Shields, G.A., Strauss, H., Howe, S.S., Siegmund, H., 1999. Sulphur isotope compositions of sedimentary phosphorites from the basal Cambrian of China: implications for Neoproterozoic-Cambrian biogeochemical cycling. J. Geol. Soc. 156, 943–955. https://doi.org/10.1144/gsjgs.156.5.0943.

Spangenberg, J.E., Lavrič, J.V., Meisser, N., Serneels, V., 2010. Sulfur isotope analysis of cinnabar from Roman wall paintings by elemental analysis/isotope ratio mass spectrometry – tracking the origin of archaeological red pigments and their authenticity. Rapid Commun. Mass Spectrom. 24, 2812–2816. https://doi.org/10.1002/rcm.4705.

Sun, Y., Wiedenbeck, M., Joachimski, M.M., Beier, C., Kemner, F., Weinzierl, C., 2016. Chemical and oxygen isotope composition of gem-quality apatites: Implications for oxygen isotope reference materials for secondary ion mass spectrometry (SIMS). Chem. Geol. 440, 164–178. https://doi.org/10.1016/j.chemgeo.2016.07.013.

Tanner, D., Henley, R.W., Mavrogenes, J.A., Holden, P., 2016. Sulfur isotope and trace element systematics of zoned pyrite crystals from the El Indio Au–Cu–Ag deposit, Chile. Contrib. Mineral. Petrol. 171, 33. https://doi.org/10.1007/s00410-016-1248-6.

Taylor, R., Clark, C., Reddy, S.M., 2012. The effect of grain orientation on secondary ion mass spectrometry (SIMS) analysis of rutile. Chem. Geol. 300–301, 81–87. https://doi.org/10.1016/j.chemgeo.2012.01.013.

Torssander, P., 1989. Sulfur isotope ratios of Icelandic rocks. Contrib. Mineral. Petrol. 102, 18–23.

Ueda, A., Sakai, H., 1984. Sulfur isotope study of Quaternary volcanic rocks from the Japanese Islands Arc. Geochim. Cosmochim. Acta 48, 1837–1848. https://doi.org/10.1016/0016-7037(84)90037-1.

Ueno, Y., Aoyama, S., Endo, Y., Matsu'ura, F., Foriel, J., 2015. Rapid quadruple sulfur isotope analysis at the sub-micromole level by a flash heating with CoF3. Chem. Geol. 419, 29–35. https://doi.org/10.1016/j.chemgeo.2015.10.032.

Ushikubo, T., Williford, K.H., Farquhar, J., Johnston, D.T., Van Kranendonk, M.J., Valley, J.W., 2014. Development of in situ sulfur four-isotope analysis with multiple Faraday cup detectors by SIMS and application to pyrite grains in a Paleoproterozoic glaciogenic sandstone. Chem. Geol. 383, 86–99. https://doi.org/10.1016/j.chemgeo.2014.06.006.

Whitehouse, M.J., 2013. Multiple sulfur isotope determination by SIMS: evaluation of reference sulfides for δ33s with observations and a case study on the determination of Δ36S. Geostand. Geoanal. Res. 37, 19–33. https://doi.org/10.1111/j.1751-908X.2012.00188.x.

Wilson, M.R., Kyser, T.K., Fagan, R., 1996. Sulfur isotope systematics and platinum group element behavior in REE-enriched metasomatic fluids: a study of mantle xenoliths from Dish Hill, California, USA. Geochim. Cosmochim. Acta 60, 1933–1942. https://doi.org/10.1016/0016-7037(96)00069-5.

Woodhead, J.D., Harmon, R.S., Fraser, D.G., 1987. O, S, Sr, and Pb isotope variations in volcanic rocks from the Northern Mariana Islands: implications for crustal recycling in intra-oceanic arcs. Earth Planet. Sci. Lett. 83, 39–52. https://doi.org/10.1016/0012-821X(87)90049-5.